Temperature Dependence of the SiPMs and the front-end Electronics for AugerPrime

von

Christoph Günther

Bachelorarbeit in Physik

vorgelegt der Fakultät für Mathematik, Informatik und Naturwissenschaften
der
Rheinisch-Westfälischen-Technischen Hochschule Aachen

Vorgelegt im August 2016

Erstgutachter

Prof. Dr. Thomas Bretz
III. Phys. Institut A
RWTH Aachen

Zweitgutachter

Prof. Dr. Thomas Hebbeker
III. Phys. Institut A
RWTH Aachen

Contents

Introduction

For the Pierre Auger observatory, the world's largest observatory for the study of ultra-high energy cosmic rays, an upgrade named 'AugerPrime' is being developed. One of the aims of the upgrade is to achieve a more precise measurement of the chemical composition of the cosmic rays. Therefore the presently used water-Cherenkov surface detector will be upgraded by an additional muon detector on top called "SSD" (Scintillating Surface Detector). The detector will consist of scintillating bars read out by photosensors. As proposed by the III. Phys. Inst. A, RWTH Aachen, an efficient way to read out the scintillation light is to use silicon photomultipliers (SiPMs) instead of photomultiplier tubes (PMTs). These propose to have a higher photon detection efficiency and a wide dynamic range. The gain of the SiPMs varies with the temperature by $\approx 2\,\%$ per K. In the Argentinian Pampa where the observatory is located, the temperature differs from ≈ -20 to $40\,°\mathrm{C}$. Therefore a compensation of the temperature dependence is needed. This can be achieved by adjusting the bias voltage applied to the SiPMs.

Aim of this thesis is to empirically determine this temperature dependency of the gain. Based on the results of the measurements an automated stabilisation of the gain is tested. This thesis starts with an overlook over the present state of the Pierre Auger Observatory and details of the planned upgrade. Afterwards an introduction about the theoretical specifications of the SiPMs, including the temperature dependency and correlated noise effects are described. Thereafter details of the performed measurements are described, seperated into the measurement setup and the analysis.

CHAPTER 1

The Pierre Auger Observatory

1.1 The Pierre Auger Observatory

The Pierre Auger Observatory is presently the largest and most accurate experiment in the world to study ultra-high energy cosmic rays (UHECRs). The UHECRs trigger air showers which development in the atmosphere can by measured by the generated secondary particles and light. Aim of the observatory is to study the sources and the chemical composition of cosmic rays at energies above 10^{18} eV. The experiment is located near Malargüe, Argentina where it spans over 3000 km^2 in the Pampa Amarilla with its 1660 surface detector (SD) stations and 27 fluorescence detectors (FD) enclosing the array. A schematic view of the observatory can be seen in figure 1.1. The SD stations consist of water-Cherenkov tanks (WCT) containing 12.000 l of ultra-pure water. Inside the tank photomultiplier tubes (PMT) are installed which detect the Cherenkov light that is emitted when a charged particle penetrates the water of the tank. The detectors can thereby measure the electromagnetic and muonic component of the cosmic rays. These are generated in the decay of charged hadronic particles such as Pions and Kaons. The most frequent reaction generating these cascades is proton-nucleus scattering of cosmic protons with atmospheric air nuclei.

The SD stations are overlooked by the FD telescopes. These can detect light emitted by nitrogen molecules in the atmosphere when excited by secondary particles within the extensive air showers. Using two different detector types offers the advantage that they can be calibrated with each other to minimize systematic errors and to be able to improve the reconstruction of the geometry of the showers. [1]

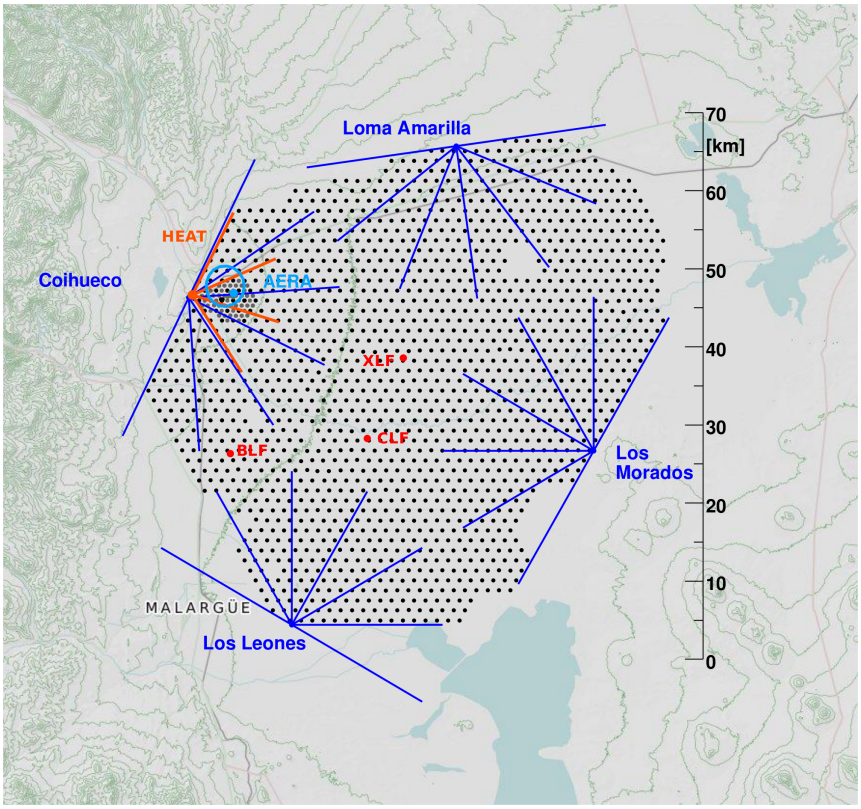

Figure 1.1: Schematic view of the Pierre Auger Observatory. The black dots represent the positions of the surface detector stations and the blue dots and lines outline the positions and the field of view of the fluorescence detectors. Taken from [1]

1.2 AugerPrime

An upgrade named 'AugerPrime' of the Pierre Auger Observatory is planned to enable a more precise analysis of the air showers. Main aspects of the upgrade are the extension of the surface stations with $4\,\mathrm{m}^2$ plastic scintillators on top and new surface detector electronics. With the new scintillating surface detectors (SSD) a improved measurement of the muon component of the cosmic rays can be achieved, as the SSD will have a different response to the components of the extensive air showers (EAS). The SSD signal will be dominated by electron signals while the WCT signals will be dominated by photons and muons. By combining both signals a separation of the components of the EAS can be achieved. [2, S.53] A picture of the prototype can be seen in figure 1.2. A prototype of this detector named ASCII (Auger Scintillator for Composition II) has already been installed in 2010. As planned for SSD, it consists of a plastic scintillator, but with a size of $2\mathrm{m}^2$. The scintillation light is coupled to a wavelength shifting fiber (WLS) and the signal is read out by a single photo detector. As proposed by III. Phys. Inst. A of the RWTH Aachen some of the ASCII modules are read out by Silicon Photomultipliers (SiPM) instead of PMTs. Advantages of SiPMs compared

Figure 1.2: Picture of the extension of the SD station with a scintillating detector on top. Taken from [2]

to PMTs are a lower operation voltage, $\mathcal{O}(60\,\mathrm{V})$ in comparison to $\mathcal{O}(2000\,\mathrm{V})$ [2, S.54], a wide dynamic range and lower costs. Challenges of using SiPMs are especially their temperature dependency of the breakdown voltage which corresponds to a decrease of the gain with increasing temperature. However as will be shown in this thesis this effect is linear and can be compensated by adjusting the supply voltage. While currently SiPMs of type MicroFC-60035-SMT by the manufacturer SensL are also used in the ASCII modules, the characteristics of SiPMs by th manufacturer Hamamatsu are studied at the III. Phys. Inst. A of the RWTH Aachen such as in this thesis. These SiPMs propose to have wide dynamic range and a high photon detection efficiency (PDE) of up to 50 %. [2]

CHAPTER 2

Silicon Photomultipliers

Silicon Photomultipliers (SiPMs) are photon counting devices consisting of hundreds to several ten thousands avalanche photodiodes operating in Geiger mode. They have capabilities similar or even better than common photomultiplier tubes (PMTs) and are therefore interesting for various fields of application such as particle physics. In this chapter a theoretical characterisation of SiPMs with focus on the characteristics studied in this thesis will be described.

2.1 Photon detection with semiconductor devices

When a photon travels through a semiconductor such as silicon, it can excite electrons from the valence band to the conduction band, creating a measureable current. The excited electron leaves a positively charged hole in behind the valence band, together called an electron-hole-pair. For silicon the gap energy between these bands is about $E_\mathrm{g} = 1.1\,\mathrm{eV}$.[21, S. 187] Therefore photons with an energy $E_\gamma = \hbar\omega \geq E_\mathrm{g}$ can be detected. To detect photons with lower energies than the band gap, photodiodes consist of layers of doped silicon. N-doped areas include additional impurities of atoms (donors) such as Phosphorus adding an additional electron state near the conduction band. P-doped areas are areas doped with atoms having one valence electron less (acceptors) such as Boron adding one positively charged state, a hole, near the valence band. At room temperatures the electrons of the donors gain a thermal energy of $E_\mathrm{T} = kT = \frac{1}{40}\,\mathrm{eV}$, being able to pass to the conduction band and leaving positively ionized donors in the valence band. Analogous the acceptor atoms can collect an electron from the valence band forming a negatively charged ion. This process is called extrinsic conduction. The charge difference between the doped areas creates an electrical field causing a drift current. In thermal equilibrium this drift cancels out with the thermal diffusion of the charge carriers resulting in a charge free zone called

depletion layer. This results in an electrical potential across the junction and an energy shift between the n- and p-layer.

Avalanche photodiodes have an additional reverse voltage V_{bias} applied to this junction. This causes an increase of the depletion zone and therefore an increase of the electrical field inside. If this field is strong enough, the electrons of the electron-hole-pairs gain enough acceleration to excite more electron-hole-pairs which will then get accelerated in the electrical field as well. In avalanche photodiodes this process is created only by the electrons because of their higher mobility compared to the holes. [21, S. 187] The charge generated by the avalanche process provides a gain of the photon signal in the order of 100.The gain is the amount of charge in units of the elementary charge e.

To reach even higher sensitivities to detect single photons, the avalanche photodiodes can be operated over their breakdown voltage V_{BD}. By doing this, electrons and also holes gain enough energy inside the electrical field of the depletion layer to create avalanches. These avalanches gain so much energy that they would diverge as long as the voltage over the diode is higher than the breakdown voltage. Therefore a quenching resistor has to be connected in series to the diode. This resistor in the range of 100kΩ to a few MΩ leads to a voltage decrease over the diode when the current created by the avalanche flows through it. When the diode voltage falls under the breakdown voltage the avalanche stops. The avalanches excited in this mode create the same amount of charge, independently of the energy of the initial photon. This process is called a breakdown of a cell. The device is therefore called a Geiger Mode avalanche photodiode (GAPD). It allows to detect single photons with a very high gain $> 10^6$ [8]. The gain is proportional to the generated charge Q of an avalanche which can be calculated by:

$$g \propto \frac{Q}{e} = \cdot C_{\text{cell}} \cdot (V_{\text{bias}} - V_{\text{BD}}) = \cdot C_{\text{cell}} \cdot V_{\text{OV}} \tag{2.1}$$

With the gain g, the capacitance C_{cell} of a cell, the reverse supply voltage V_{bias} and the overvoltage V_{OV} being the difference of supply and breakdown voltage.[14]

Because the GAPD creates a binary signal in form of equi-charged avalanches it is insensitive to the flux of the light. To solve this problem silicon photomultipliers consist of multiple GAPDs connected in parallel. A simple schematic of this circuit can be seen in figure 2.1.

The output signal of the SiPM is the sum of all the included GAPDs and allows to detect a signal with information about the flux of light reaching the cells. An example of such a signal can be seen in figure 2.2. The breakdown of multiple cells create discrete pulse integrals when added up. This pulse integral is therefore corresponding to the number of photons detected by the SiPM and is called photon equivalent (p.e.).

The pulses have a short rise time in the order of 10 ns. Their decay can be described by an exponential function $A(t) \propto \exp(-\frac{t}{\tau})$ with the time constant $\tau = R_{\text{Q}} \cdot C_{\text{cell}}$. An example of measured pulses can be seen in figure 2.3.

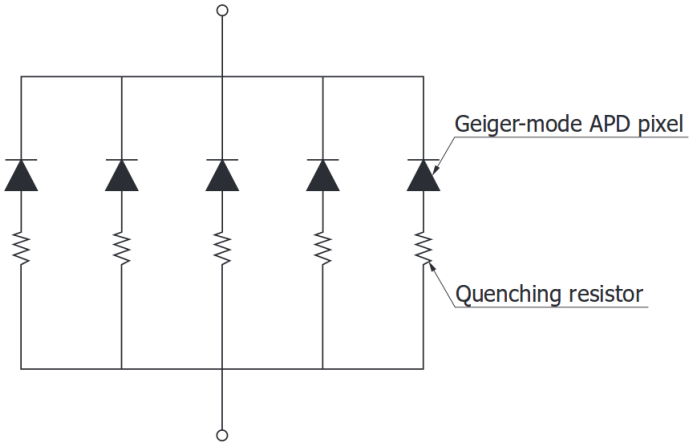

Figure 2.1: Basic structure of a SiPM. The GAPDs are connected in parallel, each connected to a quenching resistor in series. The voltage is applied reverse to the GAPDs. Taken from [14]

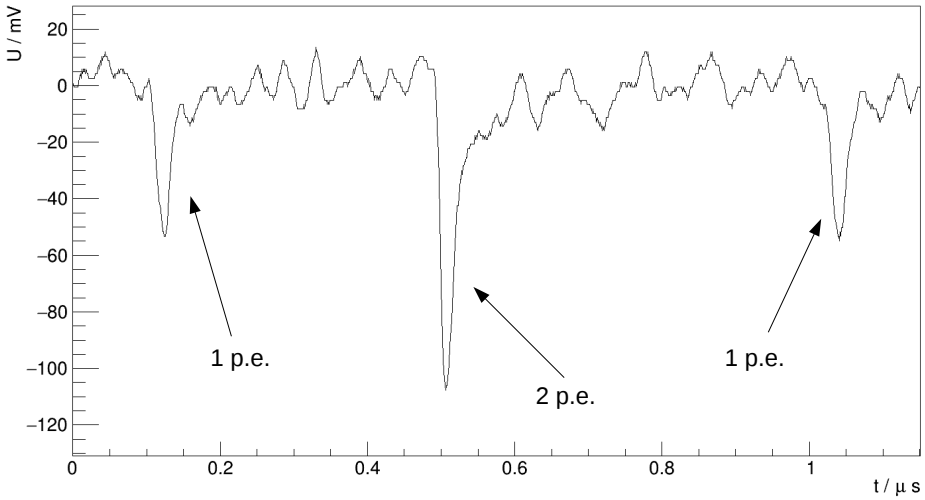

Figure 2.3: Amplified SiPM signal at 10 °C, $V_{\text{bias}} = 54.78\,\text{V}$. The pulses have discrete heights corresponding to the number of cell breakdowns (p.e.).

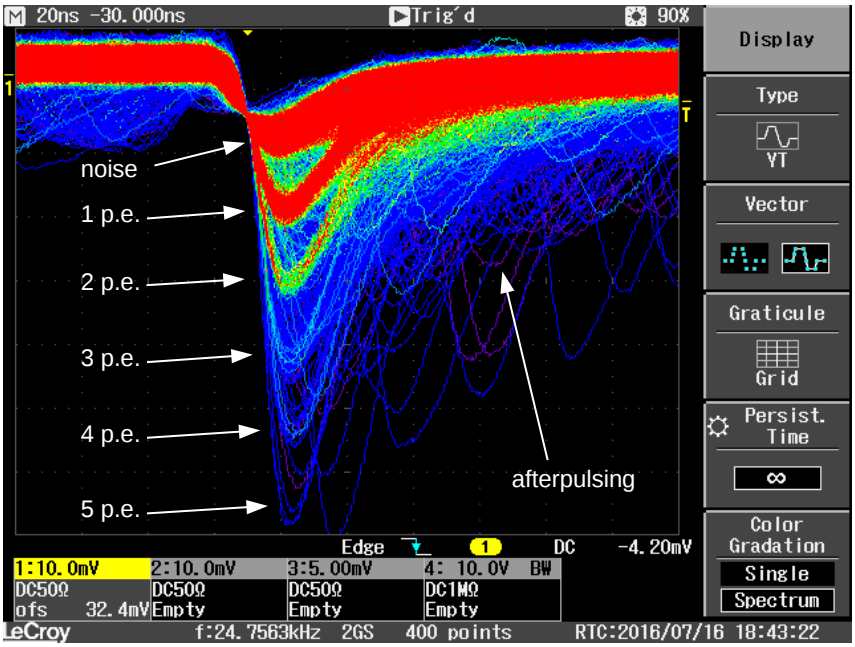

Figure 2.2: Oscilloscope screenshot of the amplified SiPM signal of Hamamatsu S13360-6050PE SiPM at −30 °C, 56 V, horizontal axis: time (division = 20 ns), vertical axis: voltage (division = 10 mV). The frequency of signals is color encoded. The different p.e. signals are visible by the different colored edges of the triggered pulses, ranging from 1 to 5 p.e. Persistent time: $> 10\,s$. More oscillograms like this and for different temperatures can be found in the appendix 9.1.

2.2 Noise effects of SiPMs

Several types of noise effects occur at SiPMs seperated to correlated and thermal noise.

Thermal noise occurs due to the fact that electrons in the valence band of the GAPD cells have a statistically distributed probability to gain enough thermal energy to generate an avalanche without being excited by a photon. Due to developments of the SiPMs the rate of this thermal excitation of cell breakdowns has been decreased to about 2000 kHz at room temperature for a SiPM size of $6 \times 6\,\mathrm{mm}^2$. The rate increases with temperature by a factor of about 2 every 10 °C as measured in this thesis 5.1.4. It also increases with the overvoltage.

Correlated noise effects are optical crosstalk and afterpulsing. Optical crosstalk describes the effect that during a cell breakdown photons are produced that can trigger another breakdown in a cell near to the initial cell. Since this process is instantaneous

the pulses add up to a $2, 3, ..$ p.e. signal. Because of this effect it is possible to see signals with more than one p.e. when measuring the dark noise of a SiPM. The rate of n p.e. signals measured decreases by about $N_0 \cdot p_{\mathrm{xt}}^n$, whereas N_0 is the rate of 1 p.e. signals and p_{xt} is the crosstalk probability. The probability of this effect increases with the overvoltage. It was significantly decreased from 44 % to 3 % by the manufacturer of SiPMs by innovations such as trenches around the cells [13].

The other effect, afterpulsing, describes the effect that charge carriers can be trapped in lattice defects of a cell during an avalanche. After a time in the order of 10 ns these charges can trigger a new avalanche called an afterpulse. In figure 2.2 afterpulses can be seen behind the triggered pulses.

Another characteristic parameter of SiPMs is their photon detection efficiency (PDE). This parameter describes the probability of the SiPM to detect an incoming photon. The PDE compounds of the geometric fill factor and the quantum efficiency. The geometric fill factor describes the ratio of sensible detection area to the full area of the SiPM surface. This includes for example the space needed for the quenching resistors and the trenches between the cells to minimize optical crosstalk. The quantum efficiency depends on the wavelength of the photons and is maximal for the SiPMs used in this thesis for UV-light with a wavelength of roughly 450 nm [8].

2.3 Temperature Dependence

The breakdown voltage of SiPMs increases with the rising temperature by about $54\,\frac{\mathrm{mV}}{\mathrm{K}}$ [13]. This corresponds to a temperature dependency of the overvoltage and thus the gain of $\approx 2\,\frac{\%}{\mathrm{K}}$. The temperature dependence of the breakdown voltage can qualitatively be understood as an energy loss of the charge carriers due to scattering with the crystal lattice by emitting phonons. Thus they need a higher electric field to acquire the energy for impact ionization and in consequence a breakdown. As previous measurements have shown, the temperature dependence can be approximated linear on a wide temperature range [11], [19]. The breakdown voltage will therefore be expressed as:

$$V_{\mathrm{BD}} = V_{\mathrm{OV}}(25\,^\circ\mathrm{C}) + \beta \cdot (T - 25\,^\circ\mathrm{C}) \tag{2.2}$$

Whereas β is the progression factor measured in $\frac{\mathrm{mV}}{\mathrm{K}}$. With equation 2.1 this translates to a temperature dependency of the gain by:

$$\frac{g}{g(25\,^\circ\mathrm{C})} = 1 - \frac{\beta}{V_{\mathrm{BD}}(25\,^\circ\mathrm{C})} \cdot (T - 25\,^\circ\mathrm{C}) \tag{2.3}$$

This means in theory that it is possible to stabilise the gain by adjusting the bias voltage with the temperature by the factor β.

The specifications given by the manufacturer are listed in the following table 1:

Model	S13360-6050PE	S13360-6025PE
Serial No.	10153	30004
V_{BD}	52.62 V	51.91 V
V_{OV}	3 V	5 V
Sensor Size	$6 \times 6\,\mathrm{mm}^2$	$6 \times 6\,\mathrm{mm}^2$
Cell size / Pitch	50 μm	25 μm
Number of cells	14400	57600
Fill factor	74 %	47 %
Crosstalk probability	3 %	1 %
PDE	40 %	25 %
Gain	1.7×10^6	7×10^5
dark counts	2000 kcps	1600 kcps
β	54 $\frac{\mathrm{mV}}{^\circ\mathrm{C}}$	54 $\frac{\mathrm{mV}}{^\circ\mathrm{C}}$

Table 1: Manufacturer specifications by Hamamatsu for 50 μm and 25 μm cell pitch SiPMs, Taken from [8]

CHAPTER 3

Measurement Setup

In this chapter the experimental setup and details of the measurement devices are described. A picture of the setup can be seen in figure 3.1 A scheme of the setup is shown in figure 3.2. All devices except the climate chamber are controlled or read out by a Raspberry Pi either by ethernet or serial connection.

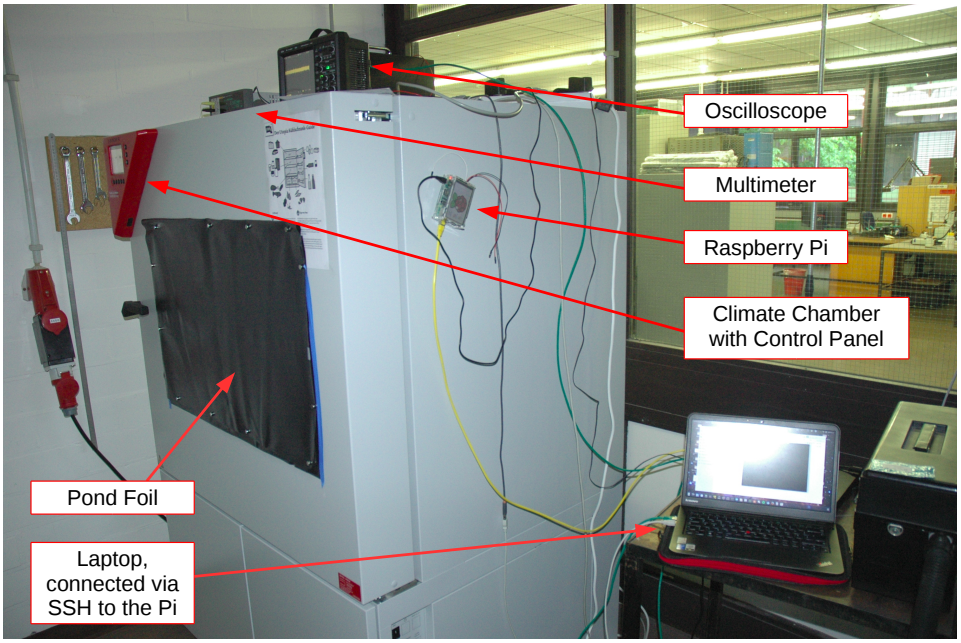

Figure 3.1: Picture of the measurement setup. The ethernet communication is provided by a switch (not shown in this picture)

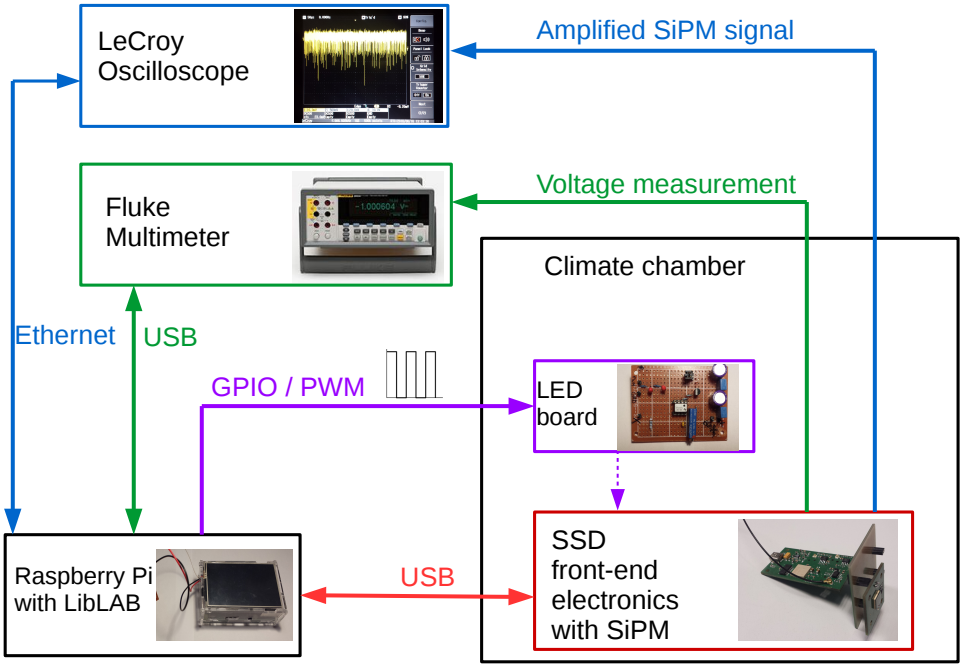

Figure 3.2: Picture of the experimental setup. Cables are lead through a light- and air-tight sluice inside the climate chamber. GPIO: General Purpose Input Output. PWM: Pulse Width Modulation.

3.1 SSD front-end Electronics

3.1.1 Amplifier Board

The SiPM signals are amplified by the amplifier board developed by J. Schumacher at III. Phys. Inst. A RWTH Aachen. SiPMs can be connected to the amplifier board by an adapter socket. Three different amplification levels are designed whereas the highest one, the calibration gain, is used for the measurements in this thesis. Besides the amplification circuit it includes the voltage supply chip and the temperature sensor. It is supplied and controlled via a USB (Universal Serial Bus) port. Two different versions of the board were used for the measurements. The newer version has a higher gain and a higher signal-to-noise ratio and enables a better analysis of the traces. As the board was still in development during this thesis, the main part of the measurements are carried out with the older version. As the measurement time with the climate chamber was limited the measurements could not be carried out again with the new version. In the following context the versions will be referred to as the 'first' and 'second' amplifier board, while 'second' corresponds to the new board and vice versa. A picture of the

second amplifier board can be seen in figure 3.3.

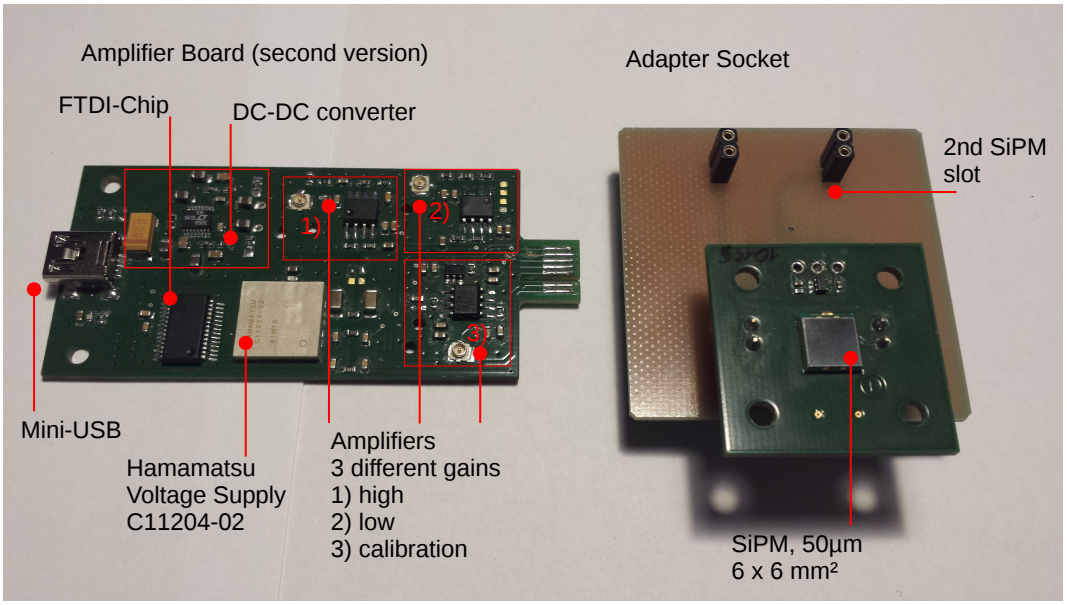

Figure 3.3: Picture of the amplifier board, second version. FTDI: Future Technology Devices International (USB to serial Chip)

3.1.2 Temperature Sensor

The temperature sensor is a Texas Instruments LM94021. It is mounted on the adapter socket of the SiPM and thus provides a measurement of the temperature close to the SiPM. It is an analog temperature sensor with a temperature range of −50 °C to 150 °C [9]. The sensor is read out by an ADC that is integrated in the power supply chip. The sensor is also used by the power supply chip for the built-in temperature compensation. The statistical error of the temperature sensor is estimated by the combination of the RMS of all temperature values recorded at one temperature and the systematic error is the digitisation of the ADC of the voltage supply chip. This value was determined from the measurement data to be $\sigma_{T,\mathrm{syst}} = 0.0035\,°\mathrm{C}$.

3.1.3 Power Supply

The power supply of the SiPMs is provided by the voltage supply chip C11204-02 by Hamamatsu [7]. It has an output range from 40 V to 90 V with an accuracy of 1.8 mV. The maximum output current is 2 mA. Voltage, current and temperature can be read

out via a serial interface. A program that provides serial connection to the supply unit was written by Prof. T. Bretz at III Phys. Inst. A RWTH and was adapted into the measurement program. A main feature of the supply unit is the built-in temperature compensation. Four factors α_i and β_i can be set to perform a change of the bias voltage V_{bias} in dependence of the temperature, given by the function:

$$V_{\text{bias}}(T) = \begin{cases} V_0 + (\alpha_1 \cdot (T - T_0)^2 + \beta_1 \cdot (T - T_0)), \text{ for } T \geq T_0 \\ \\ V_0 + (\alpha_2 \cdot (T - T_0)^2 + \beta_2 \cdot (T - T_0)), \text{ for } T < T_0 \end{cases} \tag{3.1}$$

T is the temperature measured with the temperature sensor, T_0 an arbitrary temperature at which the parameter set changes and V_0 the voltage set at temperature T_0. The manufacturer specifies a single β-factor of 54 $\frac{\text{mV}}{\text{K}}$ for the SiPMs. T_0 is set to 25 °C as this is the temperature that the manufacturer specification relates to and it is a common temperature at which the SiPMs are operated. A picture of the voltage supply chip can be seen in figure 3.3.

3.2 Climate Chamber

To provide a homogeneous and stable temperature environment, a climate chamber of type MK 240 by the manufacturer Binder was used. The chamber can be programmed via a control panel to set temperatures in a range of −40°C to 180°C and to program temperature curves [5]. For the measurements in this thesis temperatures from −40°C to 60 °C were used. To test the performance of the cooling chamber, especially the time needed to acclimate to a temperature, a test measurement is performed. The temperature is cooled down from the upper to the lower limit in steps of 10 K, with an acclimation time of 30 minutes. During the measurement, the temperature is logged by the on-board temperature sensor of the SSD front-end board in steps of 6 seconds. This time step will also be used later on to seek for temperature stability during the main measurements. Since the cooling chamber is not controlled via the measurement software, an algorithm was developed that detects when a new temperature is set by the chamber and when the temperature is stable enough to start a measurement. The algorithm saves the last 10 values (1 minute) of the temperature sensor and calculates their mean and root mean square (RMS). Temperature stability is reached when the RMS falls under a threshold-value σ_T that is determined from the test measurement. Since the temperature will always be set in steps of 10 °C the reach of a new temperature is defined as the time when the difference between the mean value at the last stable temperature and the current mean temperature is higher than 9 °C. Starting from there the algorithm calculates the RMS over 10 values until it is again lower than σ_T. The results of the test measurement can be seen in figure 3.4.

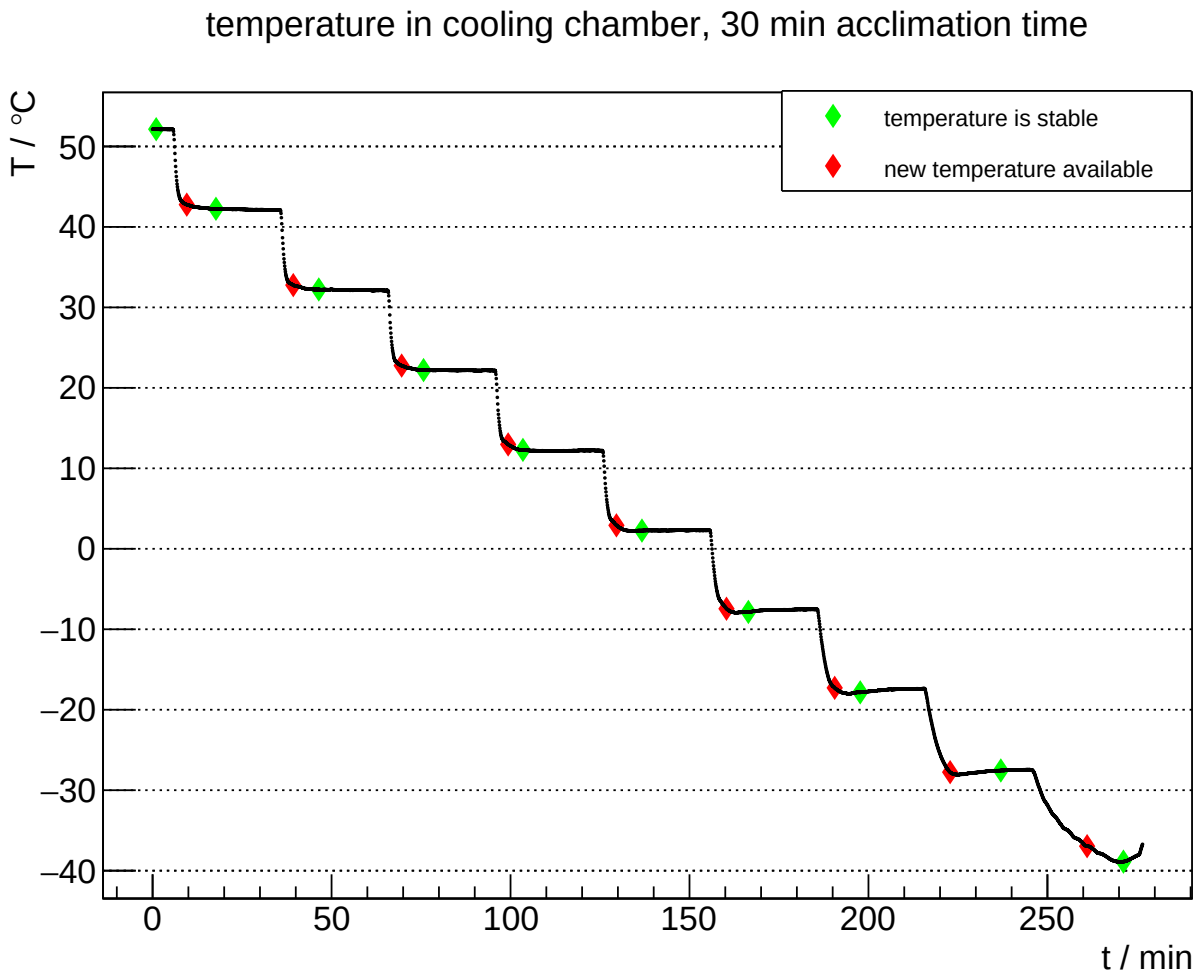

Figure 3.4: Test measurement of the climate chamber. The red triangles mark the recognition of a new temperature, the green ones mark the detection of a stable temperature. At the end of the measurement the temperature increases due to turning off the climate chamber. The offset between the fixed and the measured temperatures can be explained by a heating-up of the electronics when being turned on for a longer time.

As can be seen in figure 3.4, the algorithm detects properly the different temperature steps. The RMS-threshold is set to $0.015°C$ to achieve a compromise between a stable temperature during the measurement and a reasonable waiting time for the next temperature. The time needed by the cooling chamber to set a new temperature was estimated by this measurement to be about 15 minutes for temperatures $> -20\,°\mathrm{C}$. The time needed by the climate chamber to set temperatures increases with lower temperatures due to the higher difference to the outer temperature. Therefore an acclimation time of 20 minutes in the range of -20 to $-30\,°\mathrm{C}$ is included in the measurement time. At a temperature of $-40\,°\mathrm{C}$ the cooling chamber reaches its minimal

achievable temperature and the time needed to acclimate to this temperature becomes hard to estimate. Because this is the lowest temperature used in the measurements, the measurement time for this temperature is not set to a specific limit, but the measurement will proceed until the RMS falls below the threshold.

Since the measurements have to be carried out in complete darkness, the glass window of the cooling chamber was sealed light-tight. For this purpose pond foil turned out to be ideal. The 0.5 mm thick rubber foil was attached broadly in four layers on the window with magnets and additionally sealed with isolation tape at the edges. With each layer the rate of SiPM pulses decreased while no more significant difference between three and four layers was observable.

3.3 Oscilloscope

An oscilloscope of type WaveJet 354A by LeCroy was used to record the amplified SiPM signals. The four-channel oscilloscope has a digital 8-Bit resolution on the selected voltage range and a DC gain accuracy of $\pm(1.5\,\% \cdot V_{out} + 0.5\,\% \cdot fullrange)$, whereas V_{out} is the measured voltage value [17]. The voltage range was set individually in dependence of the temperature and overvoltage, ranging from 5 to 50 $\frac{\mathrm{mV}}{\mathrm{Div}}$. For the measurements a sampling rate of 1GS is used in correspondance to a pulse length of $\approx 50\,\mathrm{ns}$ (figure 4.3). The hardware control framework 'LibLAB' allows to read out the oscilloscope via Ethernet. This C++ library is being developed at the III. Phys. Inst. RWTH A/B [18]. The maximum number of 500.000 samples is read out for each trace.

3.4 Multimeter

Voltage measurements are performed with the 6.5 digit precision multimeter of type 8846A by Fluke. This multimeter has an input impedance of 10MΩ and was used in ranges 1 V, 10 V and 100 V. The accuracy at these ranges is given in table 2. [12]

Range	Accuracy
1V	$0.000025 \cdot V_{\mathrm{measurement}} + 7\,\mu\mathrm{V}$
10V	$0.000024 \cdot V_{\mathrm{measurement}} + 50\,\mu\mathrm{V}$
100V	$0.000038 \cdot V_{\mathrm{measurement}} + 600\,\mu\mathrm{V}$

Table 2: Accuracy of the multimeter for different voltage ranges

The multimeter data can be read out via a serial connection. Software to control the multimeter is included in the LibLAB library and was adapted to the measurement program.

3.5 LED Board

Since the SiPMs characterised in this thesis all have a low crosstalk probability $< 10\%$, pulses of high p.e. are only rarely observed in complete darkness. Therefore a LED-board was designed to be able to provide the SiPM with controllable, minimal amount of light. A LED of wavelength 400nm was used, because the SiPM has its maximal photon detection efficiency in this wavelength range. Optionally a red LED can be used by switching a jumper position. The circuit of the board is shown in figure 3.5. The board needs a supply voltage of 5V and the LED brightness can be controlled by a PWM (pulse width modulation) signal. Both are provided by the Raspberry Pi. The circuit was designed in personal correspondance with J. Schumacher at III Phys. Inst. A RWTH. A picture of the LED board is shown in figure 3.6.

To improve noise immunity against distortions caused by the 5V output rail of the Raspberry Pi, the supply voltage is filtered by two low-pass filters consisting of two $47\,\mu$H inductors and two $220\,\mu$F electrolyte capacitors. This corresponds to a filter frequency of $\approx \frac{1}{2\cdot\pi\cdot\sqrt{L\cdot C}} \approx 1.6\,$kHz. Inductors are used instead of resistors to minimize the voltage drop over the filters.

To flatten the PWM signal, it is filtered by two low-pass filters consisting of two $10\,\text{k}\Omega$ resistors and two $1\,\mu$F ceramic capacitors. This corresponds to a filter frequency of $\frac{1}{2\cdot\pi\cdot R\cdot C} \approx 16\,$Hz. Ceramic capacitors are used to minimize ripple on the output signal.

The flattened PWM signal regulates a voltage controlled current source circuit consisting of an operational amplifier (OPAmp) and a bipolar transistor. The amplifier is of type TLC272CP by Texas Instruments [10] and is supplied by the 5V input. It has an input impedance of $10^{12}\Omega$ and a differential voltage amplification of typically $A = 23\,\frac{\text{V}}{\text{mV}}$ at $25\,°$C. The transistor is a BC547 by Fairchild with a current amplification of $h_{\text{fe}} = 420 - 800$. [6]

The PWM signal is applied to the non-inverting input of the amplifier. The output of the amplifier drives the base of the transistor $Q1$ via the resistor R_3.

The current I_{e} through the LED can be calculated as followed: When the base current of the transistor is I_{b}, the emitter current is due to the current amplification of the transistor

$$I_{\text{e}} = I_{\text{b}} \cdot \left(1 + \frac{1}{h_{\text{fe}}}\right)$$

When a voltage U_{in} is applied to the input of the amplifier, the transistor is driven by the OPAmp until the voltage drop over R_5 and R_{poti} is equal to U_{in}. By approximating an equal potential at the output of the of the OPAmp and the emitter, the voltage over R_5 and R_{poti} is

$$\frac{A}{1+A} \cdot U_{\text{in}}$$

With

$$U_\mathrm{e} = (R_5 + R_\mathrm{poti}) \cdot I_\mathrm{e}$$

and under the approximation of high gains of the amplifier and the transistor, one can derive the relation:

$$\frac{I_\mathrm{a}}{U_\mathrm{in}} = \frac{A}{1+A} \cdot \frac{1}{R_5 + R_\mathrm{poti}} \cdot \frac{h_\mathrm{fe}}{1+h_\mathrm{fe}} \overset{A,h_\mathrm{fe}\gg 1}{\approx} \frac{1}{R_5 + R_\mathrm{poti}} \tag{3.2}$$

Accordingly the base current of the transistor and thus the current through the LED can be calculated by this equation. Computations of the circuit are adapted from [16].

The light efficacy of the LED in units of lm per Watt in dependence of the current can be adapted from the datasheet [15, S.7]. In a range of $0 - 1\,\mathrm{mA}$ the efficacy shows a linear dependence ranging from $0 - 0.16\,\frac{\mathrm{lm}}{\mathrm{W}}$. According to IV-curve the voltage drop over the diode is approximately $2.85\,\mathrm{V}$. With a maximum voltage of $5\,\mathrm{V}$ the resistor R_5 is chosen to $1\,\mathrm{k\Omega}$. The potentiometer has a maximum resistance of $10\,\mathrm{k\Omega}$ and is set by default to $3\,\mathrm{k\Omega}$. This enables shift the controllable current range coarsly down to lower or higher values. The fine adjustment can then be performed by the duty cycle of the PWM signal without having to access the measurement setup.

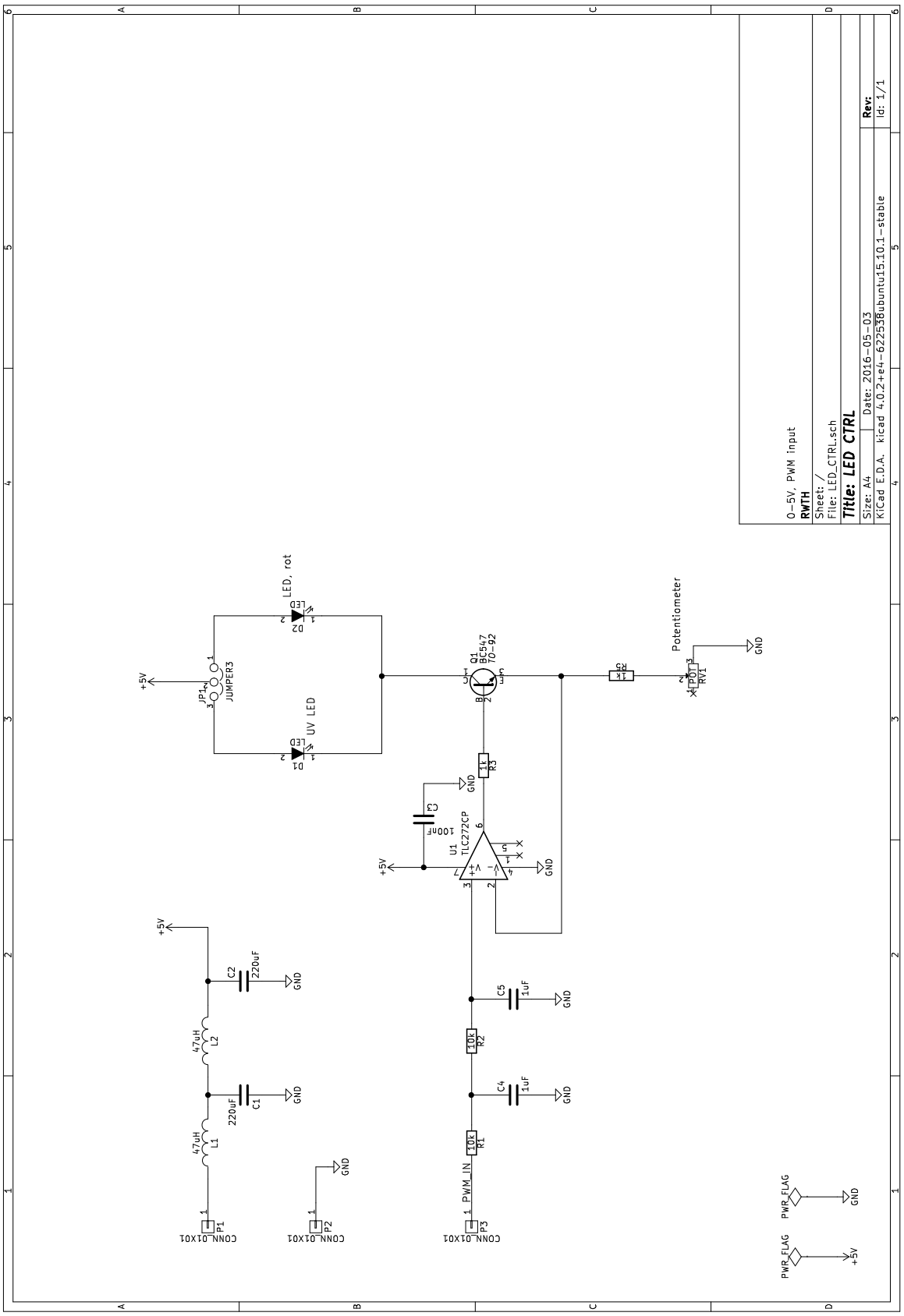

Figure 3.5: Schematic of the LED-board

3.6 Raspberry Pi

To control all the needed measurement devices and to be able to perform an automatised measurement a Raspberry Pi 3 [20] was used. The before mentioned 'LibLab' library enables the communication with all necessary devices via Ethernet or USB. The Raspberry Pi was equipped with a 3.5" touch display to be able to view the output of a running measurement program. Moreover the Raspberry Pi provides a $5V$ source and a PWM output to control the LED-board. The PWM signal can be controlled via the C++ library 'wiringPi' [22]. A picture of the Raspberry is shown in figure 3.6.

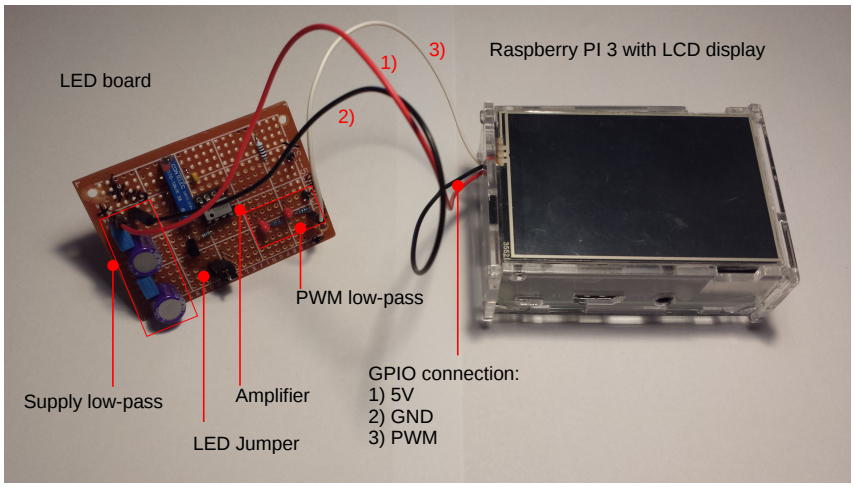

Figure 3.6: Picture of the Raspberry Pi connected to the LED board. The LEDs of the LED board are mounted on the opposite side to enable a better positioning in front of the SiPM. For the measurements the connection wires are extended.

CHAPTER 4

Peak Finding Algorithm

To be able to extract charge equivalents of the pulses in the recorded SiPM oscilloscope traces and to create pulse height spectrums (finger spectrums), a peak finding algorithm was developed. It is written in C++ and uses functions of the data analysis framework ROOT [4].

4.1 General Functionality

First of all the notation of pulse characteristics is as followed. Although the measured pulses are negative, the negative extremum of a peak will be specified as the peak. The part of the pulse from its start to the peak will be specified as the rising side. The part of the pulse behind the peak will be specified as the decaying side. A graphic representation of the algorithm can be seen in figure 4.1. To detect SiPM pulses in the data, different criteria are implemented:

The first criteria is the slope and length of a pulse. Since the SiPM pulses are of longer duration and higher amplitude than the electronic noise, the start point from where a possible pulse is further investigated, is set at the index i_0 of the trace data array where the difference between $U[i_0 + N_{\text{slope}}]$ and $U[i_0]$ is smaller than the threshold value Δ_{min}. Δ_{min} is chosen in correspondence to the amplifier gain to either $-4\,\text{mV}$ or $-35\,\text{mV}$. All further parameters and their values are listed in table 3.

If this criteria is fulfilled, a baseline before the pulse is searched, starting at the index i_0. In this context a baseline is defined as a number of $N_{RMS} = 40$ points where the RMS of the voltage values is lower than the value RMS_{thresh}. This value has to be chosen rather high, because of the electronic noise. In a range of $N_{\text{base}} = 300$ samples before the start index i_0 a window of length N_{RMS} is moved by $\frac{N_{RMS}}{2}$ in negative time direction and the RMS is calculated over the points in this window. If the RMS is lower than the threshold value the loop breaks and the mean value $V_{baseline}$ of the last

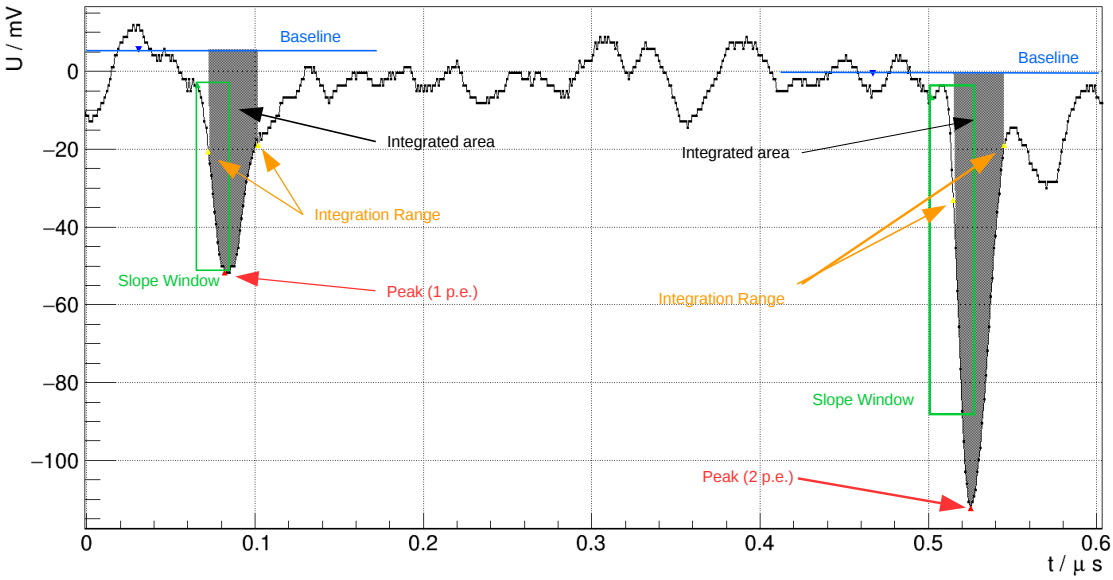

Figure 4.1: Graphical illustration of the peak finding algorithm. Zoomed into a SiPM trace recorded with the new amplifier board at $T = 10\,°\mathrm{C}$, $V_{\mathrm{bias}} = 54.81\,\mathrm{V}$. The markers and arrows mark the points where the algorithm detects characteristic positions of a pulse as described in the text.

window is saved as the baseline value.

If a baseline is found, the next step is to search for the peak. Therefore a window of $N_{\mathrm{peak}} = 15$ samples is moved in positive time direction starting at i_0. Since this point is on the rising side of the peak, the slope on this side is negative and therefore the difference between the last and first value of the window is negative. The window is moved in steps of the half window length until the slope becomes positive. The index of the peak position a is then determined by the minimum of the window in which the slope is positive for the first time. If two points in the window have the same value, the earlier one is taken. If after a number of $N_{peakwindow} = 20$ window shifts no peak was found, the pulse is refused and the detection for pulses starts again.

If the peak position and a baseline is found the difference between the peak height and the baseline value is calculated and compared to a value $V_{peakthresh}$, which is read out manually for each temperature. It is determined to detect a minimal amount of noise with an amplitude lower than one p.e.

If the peak fulfils all the criteria, the integral over the peak is calculated corresponding to the found baseline. By testing different integration lengths, it was found out, that an integration range of $i_{\text{peak}} - 10..i_{\text{peak}} + 20$ (30 ns) delivers reasonable results for all the traces. In this interval most of the pulse is included without integrating over electronic noise before and after the pulse (figure 4.1). The area under the pulse is calculated by:

$$\text{Pulse Integral} = \sum_{j=-10}^{j=20} \frac{1}{2} \cdot (V[i_{peak}+j+1] - V[i_{peak}+j] - V_{baseline}) \cdot (t[i_{peak}+j+1] - t[i_{peak}+j])$$

This integration method is used to minimize systematic errors caused by electronic noise, since oscillations of frequencies $f_{\text{noise}} > \frac{1}{30\,\text{ns}} \approx 33\,\text{MHz}$ should be cancelled out over the integration range.

After a pulse is detected, the index is increased as long as the difference between $V[i+5]$ and $V[i]$ is positive, starting at the detected peak position. This ensures that a pulse can not be detected twice. The pulse integrals are saved to a text file for further analysis.

4.2 Noise Counteraction

In some traces measured with the first electronics, noise in form of high spikes with ensuing oscillations appeared with a frequency of $\approx$ 25kHz as can be seen in figure 4.2. The noise appeared randomly and could not be correlated to parts of the measurement setup. Possible noise sources were investigated such as different voltage supplies of the Raspberry Pi and a seperate power socket for the oscilloscope with no affect on the noise. Therefore the disturbances were presumably transmitted through the electrical grounding since the measurements were carried out in an experimental hall where much electrical machinery is installed. More exact information about the sources could not be found. The noise pulses have similar amplitudes and slopes as the SiPM pulses and are therefore misinterpreted by the algorithm. Therefore methods are implemented that detect the oscillations to skip them. The first one is a threshold parameter V_{spike} that is determined from the affected traces individually. If the voltage at a point in the trace is higher than this threshold, the last two detected pulses are neglected and the index is increased by 500 (500 ns) to skip oscillations after the spike. An example for the oscillations can be seen in figure 4.3.

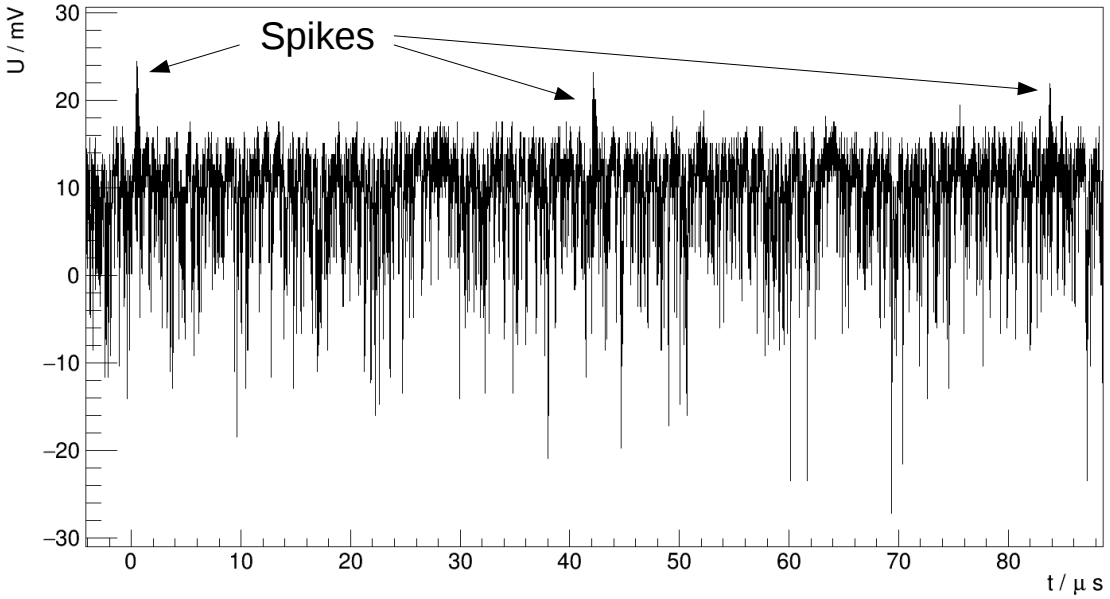

Figure 4.2: Periodical noise in form of spikes. $T = 40\,°\mathrm{C}$, $57\,\mathrm{V}$. A zoom into one of the sipkes can be seen in figure 4.3

Since not all of the oscillations could be detected by this criterion, another detection method is implemented. This is to calculate the number of change of signs of the slope N_{osc} behind a found pulse. Starting at the peak position a, the difference $|U[a+10] - U[a]|$ is calculated. If this difference is greater than $5\,\mathrm{mV}$ N_{Osc} is increased by one and the index is increased as long as the difference fulfils the criterion. This detection of change of signs is continued over $200\,\mathrm{ns}$ behind the pulse. Oscillation could be detected by neglecting pulses with more than $N_{\mathrm{osc,\,max}} = 7$ change of signs behind the pulse.

Another feature that complicates the peak finding is the increasing dark count rate of the SiPMs at high temperatures. This rate doubles about every $10\,\mathrm{K}$ resulting in a rate of $\approx 4000\,\mathrm{kHz}$ at $40\,°\mathrm{C}$. This again leads to a stacking of the SiPM pulses resulting in an unstable baseline and an asymmetry of the pulse integral. This leads to a widening of the fingers in the finger spectrums at temperatures of $30\,°\mathrm{C}$ and higher.

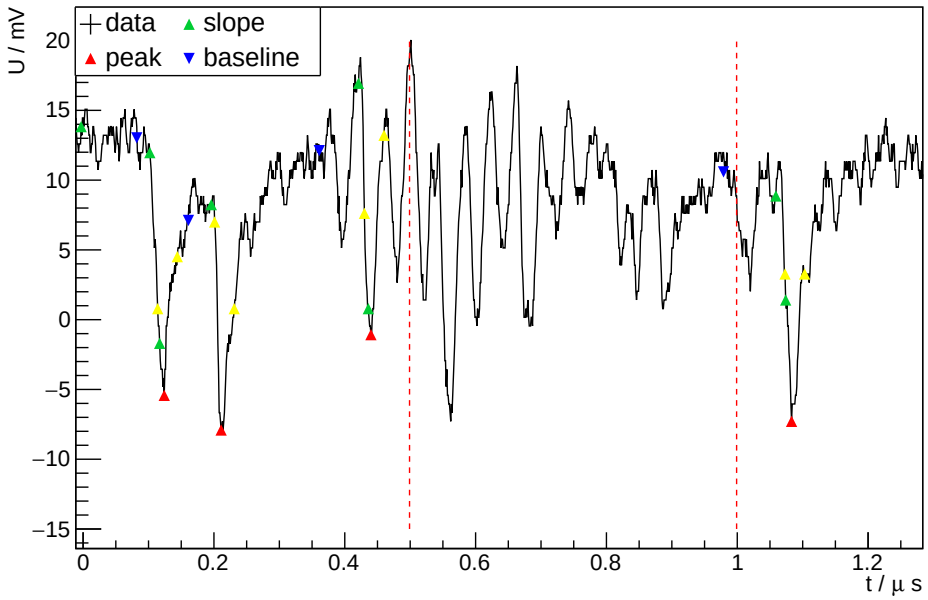

Figure 4.3: Detected oscillating noise marked by the red lines. The data 500 ns after the detection is neglected such as the detected pulse before the red line. $T = 40\,°\mathrm{C}$, 57 V, $V_{spike} = 18\,\mathrm{mV}$.

To reduce this effect additional criteria have been added. If the slope before or behind a detected peak changes its sign in the integration range the pulse is neglected. The slope is calculated by the difference between every fifth sample. Furthermore the points where the peak reaches its half peak height are calculated. Only peaks with a distance of $> 20\,\mathrm{ns}$ between these points are accepted.

Parameter	typical value	Description
N_{slope}	20	number of samples between slope is calculated
Δ_{min}	$-4\,\text{mV}$, $-30\,\text{mV}$	minimal difference between N_{slope} samples (old and new amplifier board)
N_{RMS}	40	number of samples to calculate RMS for baseline
N_{baseline}	300	maximal number of samples to look for baseline
RMS_{thresh}	2mV	threshold for baseline detection
$V_{baseline}$		mean baseline value calculated individually
N_{peak}	15	number of samples to seek for peak
$N_{peakwindow}$	20	number of shifts of the peak finding window
$V_{peakthresh}$	$-5.. - 8\text{mV}$	minimal difference between peak value and $U_{baseline}$ read out manually for each temperature
$N_{\text{Osc, max}}$	7	maximal number of oscillations behind a detected pulse

Table 3: Parameters used in the peak finding algorithm, divided into blocks according to the chronological order of tasks of the algorithm. With a sample frequency of 1 GS the number of samples are equivalent to time / ns.

CHAPTER 5

Temperature Dependence of the Breakdown Voltage

The breakdown voltage of SiPMs can be measured by at least two different measurement techniques. The main aspect of this thesis is the measurement of the gain in dependence of the overvoltage. By extrapolating the gain to zero the breakdown voltage is defined as the voltage where the gain becomes zero. Another method is to measure the IV-curve in dependence of the temperature. In this method the breakdown voltage is determined from the maximum in the $\frac{d\log(I)}{dV}$ curve.

Similar SiPMs have already been characterized using these methods [19]. For both methods a linear dependence of the breakdown voltage with the temperature has been observed.

5.1 Gain Method

The gain of a SiPM is proportional to the overvoltage as expressed in equation 2.1. The breakdown voltage is expected to increase linearly with increasing temperature as expressed in equation 2.2. Therefore the overvoltage and in consequence the gain decreases with higher temperatures. By measuring the gain for different bias voltages, the breakdown voltage is determined from extrapolating the gain, as a function of the bias voltage, to zero. By measuring the breakdown voltage for different temperatures the progression factor β can be determined.

5.1.1 Measurement Procedure

The measurement is carried out with a SiPM with a pitch size of 50μm. It is connected to the amplifier board and is placed in the light-tight climate chamber. The amplified signal is read out by the oscilloscope and the voltage supply chip is controlled via a USB

port by the Raspberry Pi as shown in figure 3.2. The temperature is decreased from 60 °C down to −40 °C in steps of 10 K. For each temperature the supply voltage is set to 11 different values and for each voltage 100 oscilloscope traces are recorded. Every time before a new trace is recorded, the bias voltage, the current and the temperature is read out from the voltage supply unit and saved to a logfile. The traces are recorded in time intervals of 2 seconds, including the buffer time for saving the data. As a reference for the voltage ranges the manufacturer specification was used as listed in table 1. A voltage range of 2 V is chosen from $V_{\mathrm{OP}}^{\mathrm{Ham}} - 0.6\,\mathrm{V}$ to $V_{\mathrm{OP}}^{\mathrm{Ham}} + 1.4\mathrm{V}$. The lower limit was estimated in test measurements showing that for lower voltages no more signal extraction was possible due to the decreasing signal to noise ratio. The upper limit was chosen so that the voltage limitation of the manufacturer was not exceeded. Since a temperature dependence of the breakdown voltage is expected the voltage range was shifted by the progression factor given by the manufacturer. The set voltages are calculated by:

$$V_{bias}(T, i) = V_{\mathrm{OP}}(25\,^{\circ}\mathrm{C}) + (i - 3) \cdot 0.2\,\mathrm{V} + 54\,\frac{mV}{K} \cdot (T - 25\,^{\circ}\mathrm{C}), \quad i = 0..10$$

With $V_{\mathrm{OP}}(25\,^{\circ}\mathrm{C}) = 52.62\,\mathrm{V} + 3\,\mathrm{V} = 55.62\,\mathrm{V}$.
A flowchart of the measurement steps can be seen in figure 5.1.

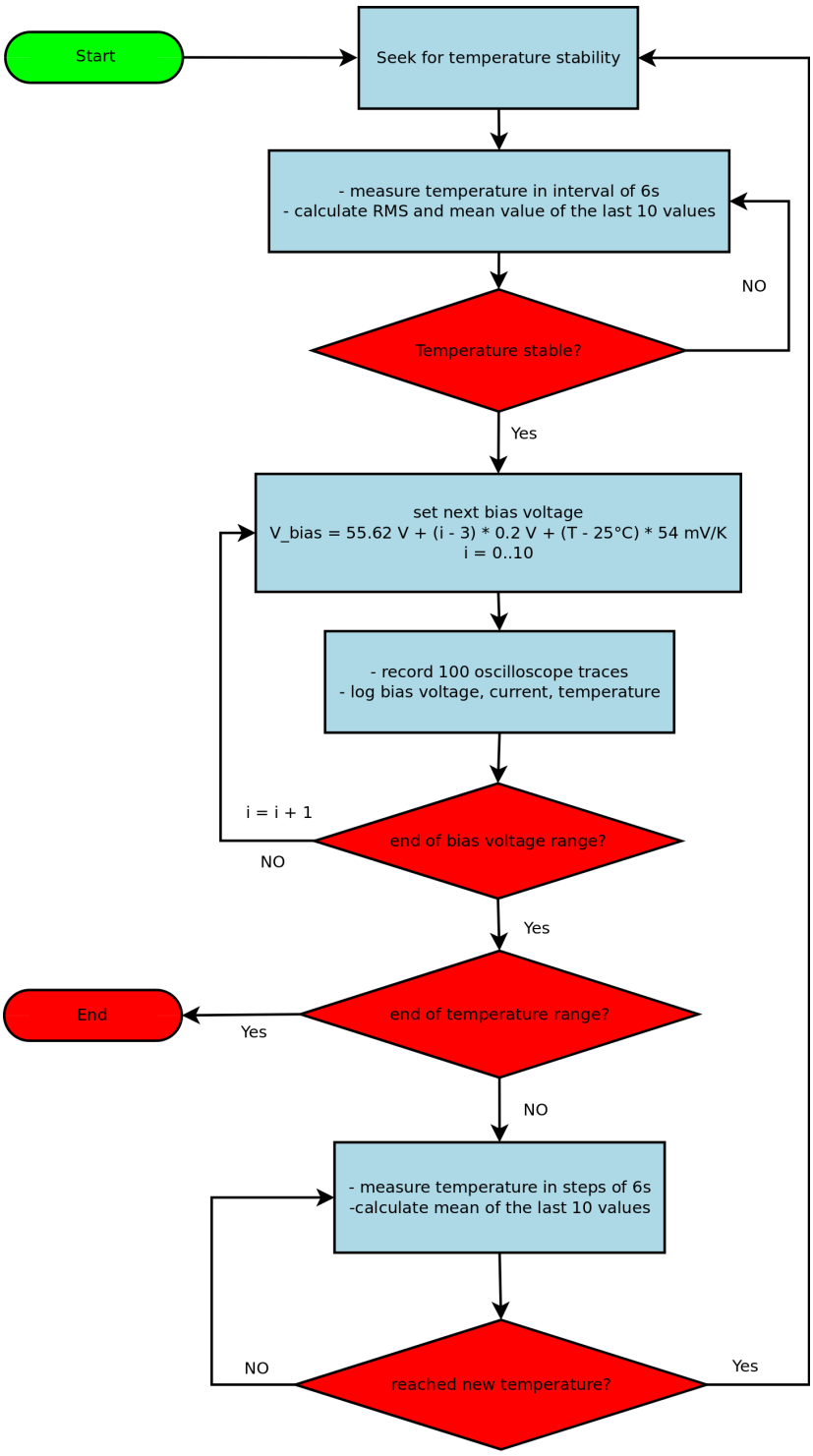

Figure 5.1: Flowchart of the measurement procedure of the gain method. A characterisation of the temperature stability is described in 3.2

5.1.2 Gain Extraction

Each dataset of 100 traces is read out by the peak finding algorithm as described in chapter 4. The extracted pulse integrals are filled into a histogram to create a finger spectrum. The gain is determined by the distance between the fingers in the spectrum. The gain is measured in units of the pulse integral, which is $\mathrm{mV} \cdot \mu\mathrm{s}$. An example of a finger spectrum can be seen in figure 5.2.

To extract the gain from a finger spectrum, the spectrum is fit by a spectrum function developed by the FACT collaboration. The function uses a sum of Gaussian functions weighted with the modified Erlang distribution. Further information and the motivation of the FACT collaboration to use this fit function can be found in [3]. Hereafter, this fit function will be called "FACT spectrum fit". The function is implemented as follows:

$$f_{\mathrm{FACT}}(x) = A \cdot \sigma_1 \cdot \sum_{n=1}^{N} \frac{e^{-\frac{1}{2}\cdot\left(\frac{x-x_n}{\sigma_n}\right)^2}}{\sigma_n} \cdot \frac{\left(n \cdot p_{\mathrm{fit}} \cdot e^{-p_{\mathrm{fit}}}\right)^{n-1}}{((n-1)!)^{\nu}} \tag{5.1}$$

A is the amplitude of the 1 p.e. finger. $\sigma_n = \sqrt{n \cdot \sigma_{\mathrm{p.e.}}^2 + \sigma_{\mathrm{el}}^2}$ is the standard deviation of the nth p.e. finger. $\sigma_{\mathrm{p.e.}}$ describes the increase of the charge fluctuations with increasing p.e. and σ_{el} describes the electronic noise. $x_n = x_0 + (n-1) \cdot g$ is the position of the nth finger consisting of a baseline shift x_0 and the gain g. The amplitudes of the fingers are weighted by the Erlang distribution parametrised by the Erlang exponent ν and the parameter p_{fit}. p_{fit} can be connected to the crosstalk probability p_{xt} as shown by simulations of the FACT collaboration [3].

To achieve reasonable and robust fit results with the function, a simplified version of the function with less parameters is fit to the finger spectrum at first. These fit results are then consigned to the FACT spectrum fit. This version of the spectrum function version will be referred to as "Pre fit". The function is parametrised as:

$$f_{\mathrm{Pre\ Fit}}(x) = A \cdot \sum_{n=1}^{N} \frac{p_{\mathrm{fit}}^n}{\sqrt{n}} \cdot \exp\left(-\frac{1}{2}\left(\frac{x - (x_0 + g \cdot (n-1))}{\sqrt{n \cdot \sigma_{\mathrm{p.e.}}^2 + \sigma_{\mathrm{el}}^2}}\right)^2\right) \tag{5.2}$$

The start values of the fit parameters and their ranges are determined individually from the finger spectrums. The fit range is set to the maximum of the finger spectrum minus 5 bins towards the end of the histogram. For the first amplifier board the histogram ranges from 0 to $1.5\,\mathrm{mV}\cdot\mu\mathrm{s}$ with a number of 150 bins. For the second amplifier board the histogram ranges from 0 to $8\,\mathrm{mV}\cdot\mu\mathrm{s}$ with a number of 300 bins. The fit is executed with the Logarithm Likelihood method implemented in the ROOT framework and the integral over the bins is fitted. The errors of the number of counts per bin are assumed to be Poissonian.

In many finger spectrums, especially the ones recorded with the first amplifier board 'background' appeared in between the fingers in the finger spectrum as can be seen in

figure 5.2. Since the traces recorded with the second amplifier board are of low noise compared to the ones of the first amplifier board and the fact that the background decreases with the second amplifier board, a possible explanation for the origin of the background could be misidentifications of pulses by the peak finding algorithm due to a low signal to noise ratio. However the background could not be removed by the implemented noise detection methods as described in chapter 4. The background could not be described by the fit functions, resulting in a mismatching of the finger positions and a high $\frac{\chi^2}{ndf}$. As a counteraction of this problem, an exponential background term is added to the fit function:

$$f_{\mathrm{bg}}(x) = A_{\mathrm{bg}} \cdot \exp\left(-\frac{x - x_{\mathrm{off}}}{\tau_{bg}}\right) \tag{5.3}$$

A motivation for the exponential dependence of the background is that the number of misidentified pulses is proportional to the number of correctly identified pulses and the rate of pulses decreases exponentially with the number of p.e. By adding the background term the space in between the fingers can be described more precisely and the positions of the fingers match better with the fit function. A comparison of the fit functions can be seen in figure 5.2.

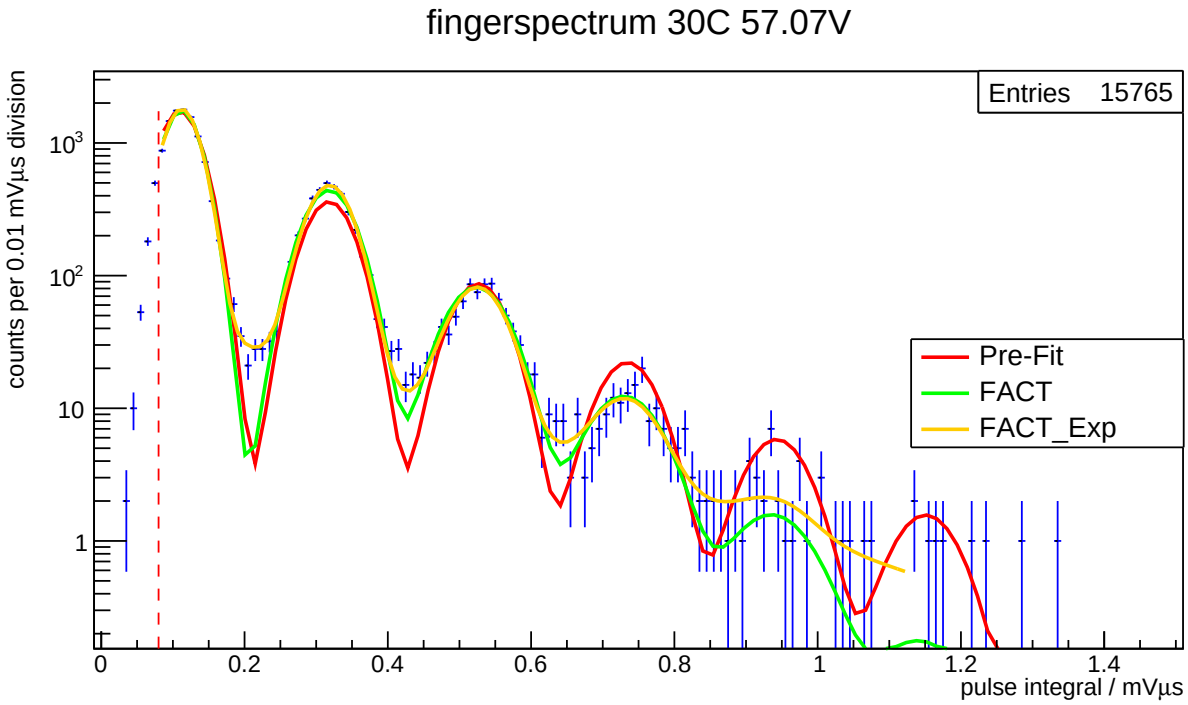

Figure 5.2: Finger spectrum fitted with different spectrum functions.

The fit results of the different functions are listed in the following table 4:

Function	Pre-Fit	FACT	FACT + Exp
A	1735 ± 20	1766 ± 20	1763 ± 23
$x_0/(\mathrm{mV} \cdot \mu\mathrm{s})$	0.10986 ± 0.00040	0.1121007 ± 0.00035	0.12246 ± 0.00033
$g/(\mathrm{mV} \cdot \mu\mathrm{s})$	0.208164 ± 0.00054	0.205800 ± 0.00053	0.20697 ± 0.00055
$\sigma_{\mathrm{p.e.}}/(\mathrm{mV} \cdot \mu\mathrm{s})$	$(2.75 \pm 0.03) \times 10^{-2}$	$(2.36 \pm 0.07) \times 10^{-2}$	$(1.87 \pm 0.076) \times 10^{-2}$
$\sigma_{\mathrm{el}}/(\mathrm{mV} \cdot \mu\mathrm{s})$	$5 \times 10^{-4} \pm 3.1 \times 10^{-3}$	$(8.05 \pm 2.50) \times 10^{-3}$	$(1.42 \pm 0.12) \times 10^{-2}$
p_{fit}	0.294 ± 0.0029	0.2126 ± 0.00515	0.20667 ± 0.000546
ν	x	1.77 ± 0.049	1.996 ± 0.07
A_{bg}	x	x	39 ± 22
$\tau_{\mathrm{bg}}/\mathrm{K}$	x	x	0.236 ± 0.016
$x_{\mathrm{off}}/(\mathrm{mV} \cdot \mu\mathrm{s})$	x	x	0.134 ± 0.131
$\frac{\chi^2}{\mathrm{ndf}}$	6.4	2.5	1.2

Table 4: Fit results of the different spectrum functions for the finger spectrum at 30 °C and $V_{\mathrm{OV}} = 4.2\mathrm{V}$

5.1.3 Measurement with the LED Board

In a test measurement the effect of measuring with minimal irradiation of the SiPM was investigated. Therefore the amplifier board with the SiPM is located in a dark box and the LED board is positioned in a distance of 2 cm in front of it. The measurement is carried out at room temperature with the first amplifier board. A picture of the measurement setup can be seen in figure 5.3.

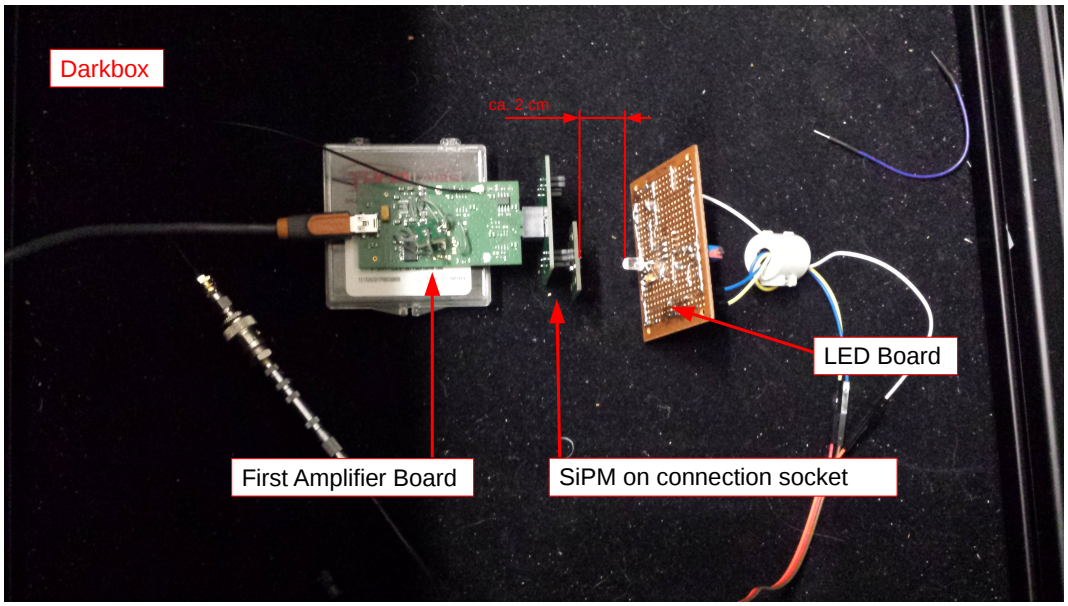

Figure 5.3: Measurement setup for the test of the LED board

100 traces are recorded with the LED turned on and off. The potentiometer is set to 6kΩ and the PWM duty cycle is set to $\frac{1}{1024}$. This corresponds to a LED current of ≈ 0.4 mA. In figure 5.5 extracts of the recorded traces can be seen.

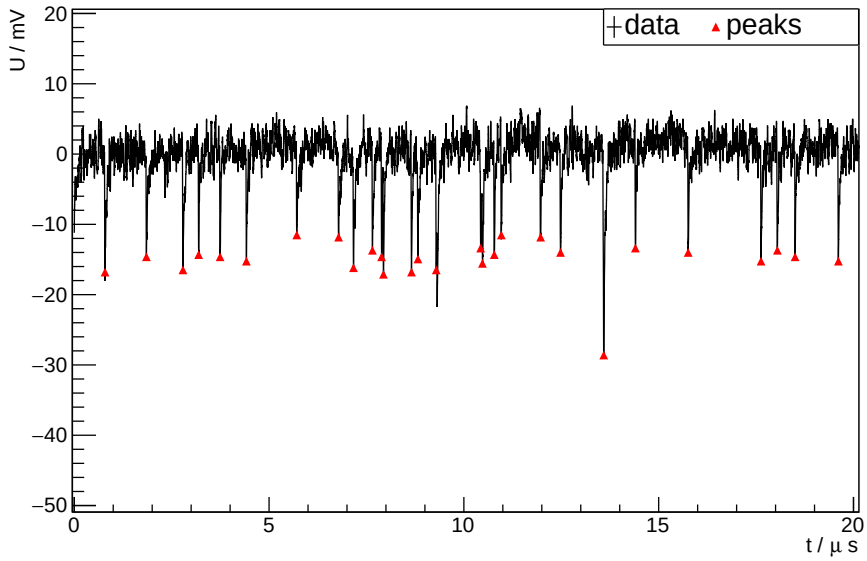

Figure 5.4: Oscilloscope trace with the LED turned off. The markers indicate detected SiPM pulses. The rate of detected SiPM pulses is $\approx 950\,\mathrm{kHz}$.

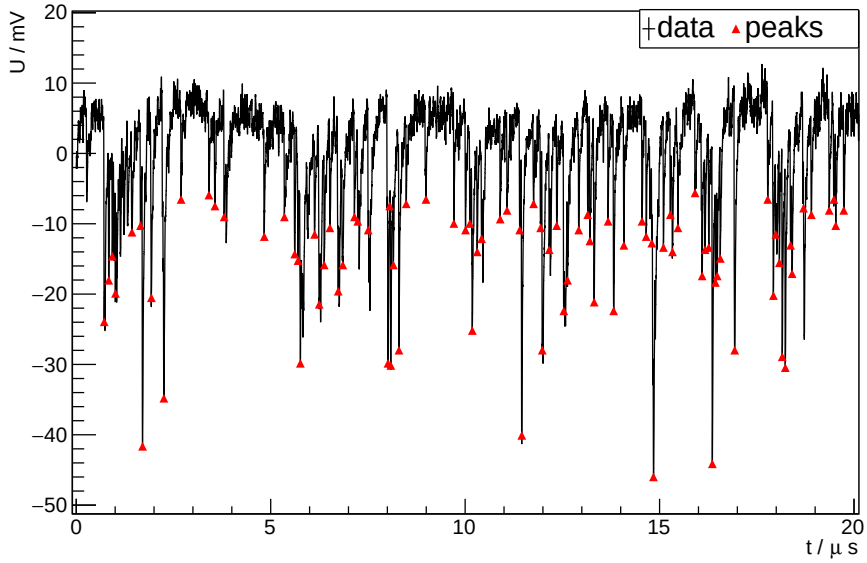

Figure 5.5: Oscilloscope trace with the LED turned on. The markers indicate detected SiPM pulses. The rate of detected SiPM pulses is $\approx 5000\,\mathrm{kHz}$.

In the traces with the LED turned on about 5 times more SiPM pulses are observed. A positive aspect is that more SiPM pulses of higher p.e. are triggered. However the

higher pulse rate leads to an increased pulse stacking. This effects the stability of the baseline and thus increases the fluctuation of the pulse integrals. 100 traces have been recorded with the LED turned on and off. The finger spectrums created from this measurement can be seen in figure 5.6.

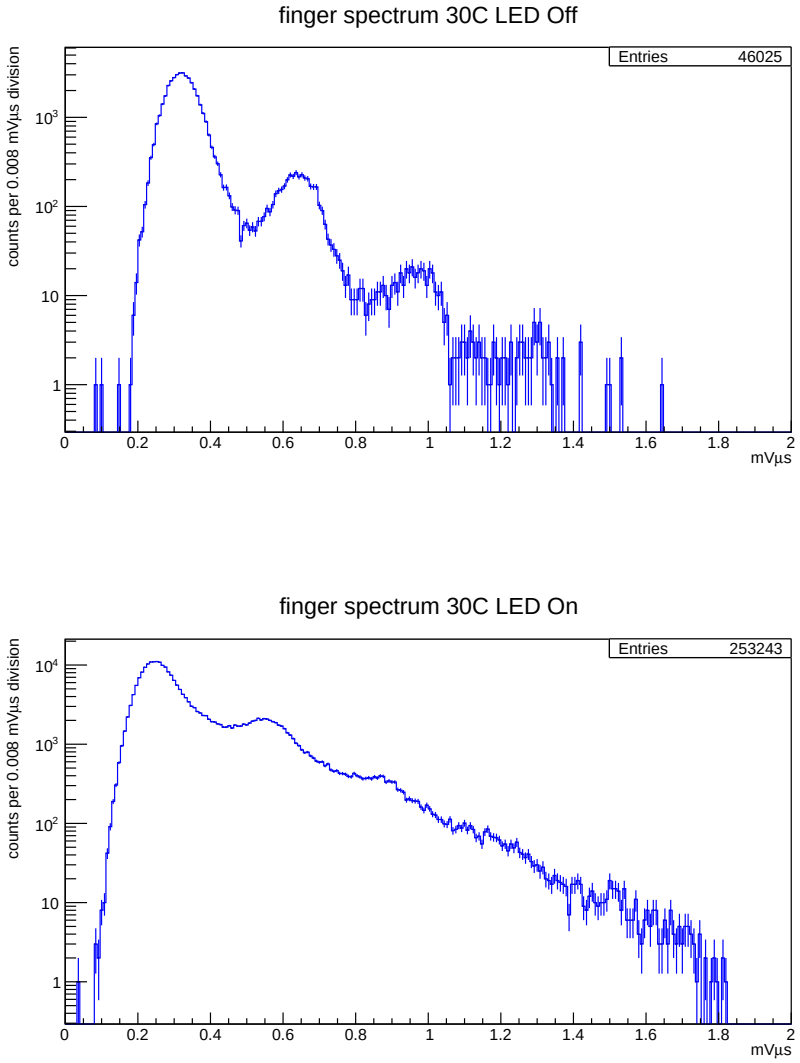

Figure 5.6: Comparison of finger spectrumsw with the LED turned on and off.

The finger spectrum with the LED turned on shows that more pulses of more than 4 p.e. are triggered. However due to the increased background the fingers can not be seperated as good as in the finger spectrum with the LED turned off. Therefore the further measurements are carried out without the LED.

5.1.4 Results Gain Method

All finger spectrums of one voltage and temperature are fitted with FACT spectrum fit with the exponential background. Examples of the finger spectrums at an overvoltage of 3.6 V can be seen in figure 5.7. An evaluation of the data is possible in a temperature range from −40 °C to 30 °C. For higher temperatures the rate of SiPM pulses increases so much that the pulses can not be detected properly by the peak finding algorithm and so the fingers can not be seperated properly enough to fit the spectrums. A graphic illustration of the resulting fit parameters can be seen in figure 5.9.

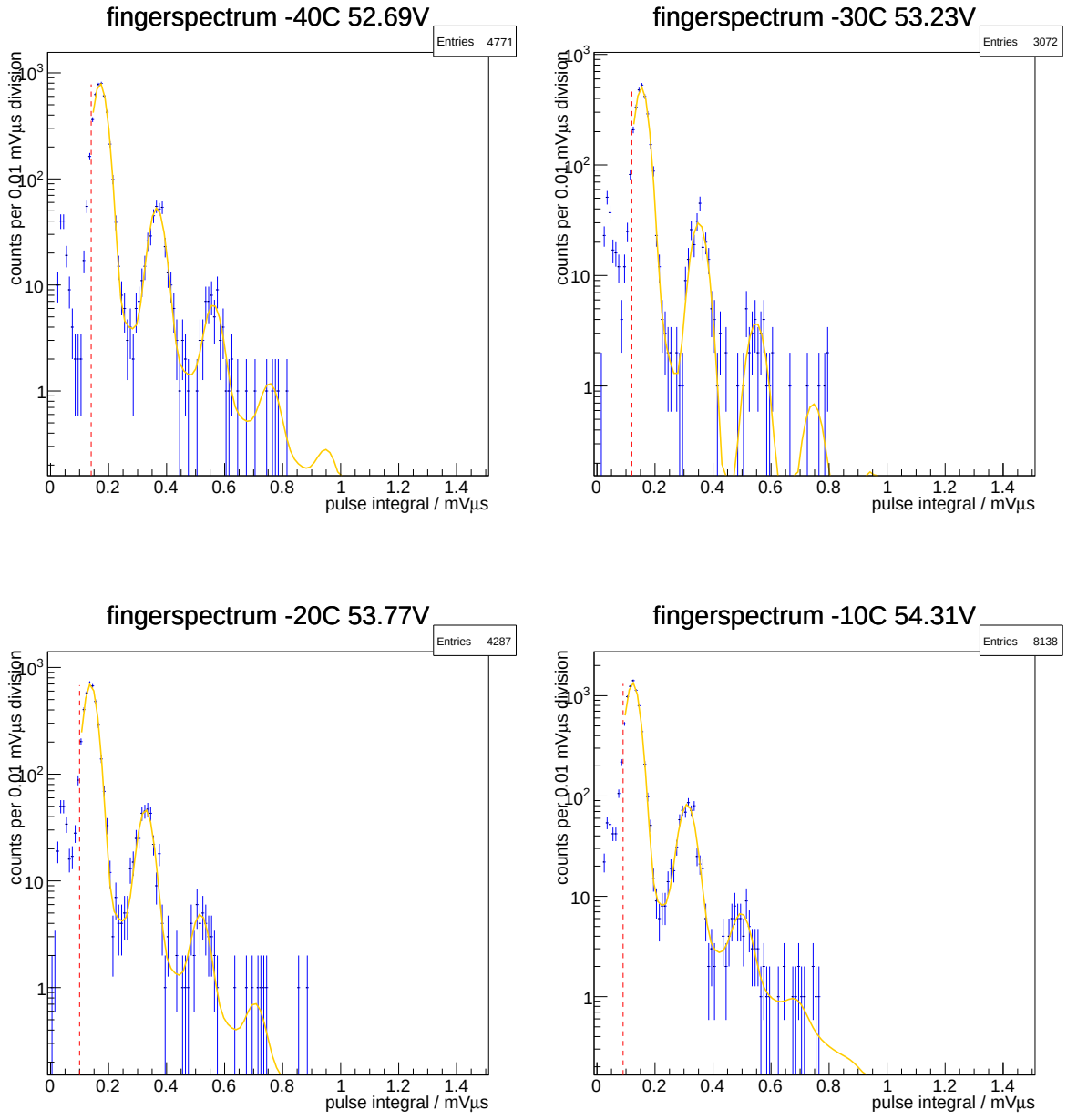

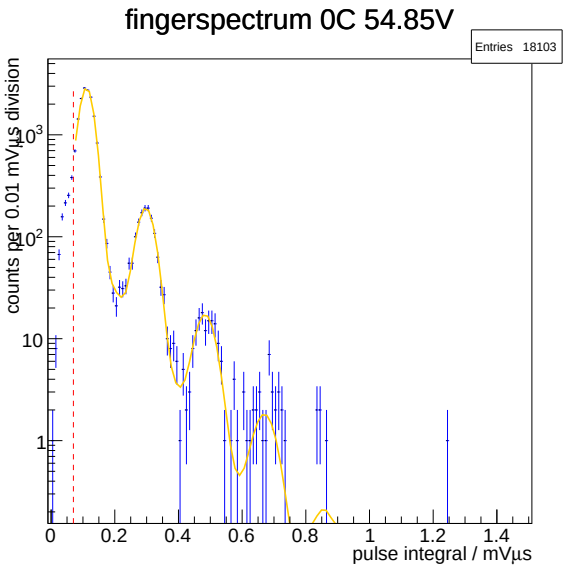
fingerspectrum 0C 54.85V
Entries 18103
counts per 0.01 mVµs division
pulse integral / mVµs

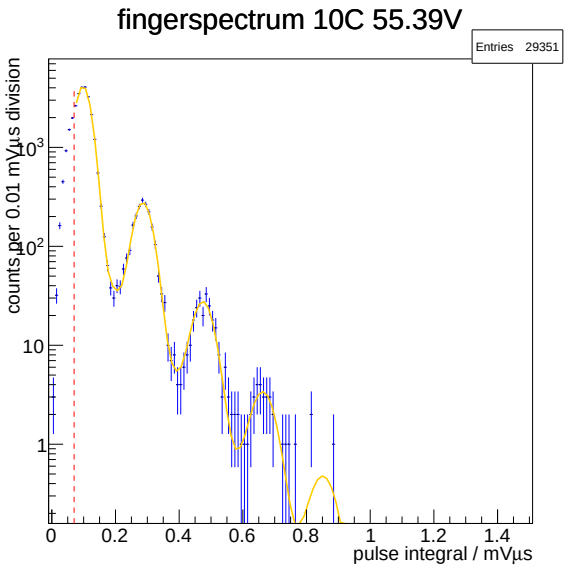
fingerspectrum 10C 55.39V
Entries 29351
counts per 0.01 mVµs division
pulse integral / mVµs

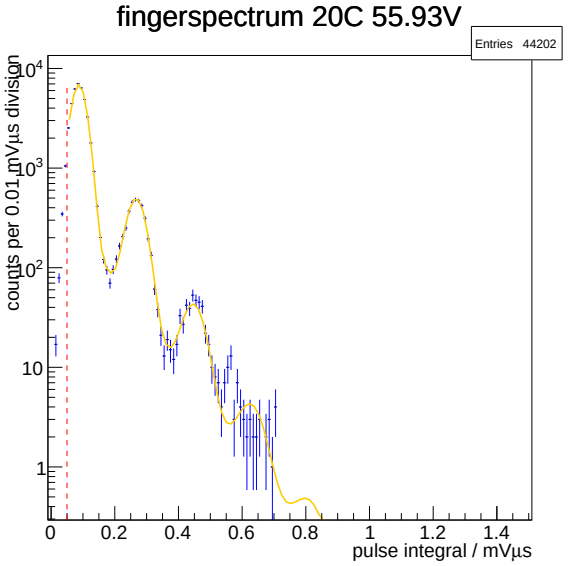
fingerspectrum 20C 55.93V
Entries 44202
counts per 0.01 mVµs division
pulse integral / mVµs

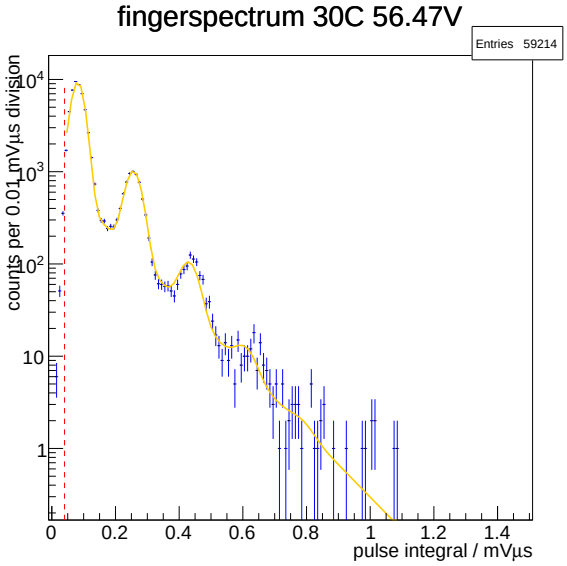
fingerspectrum 30C 56.47V
Entries 59214
counts per 0.01 mVµs division
pulse integral / mVµs

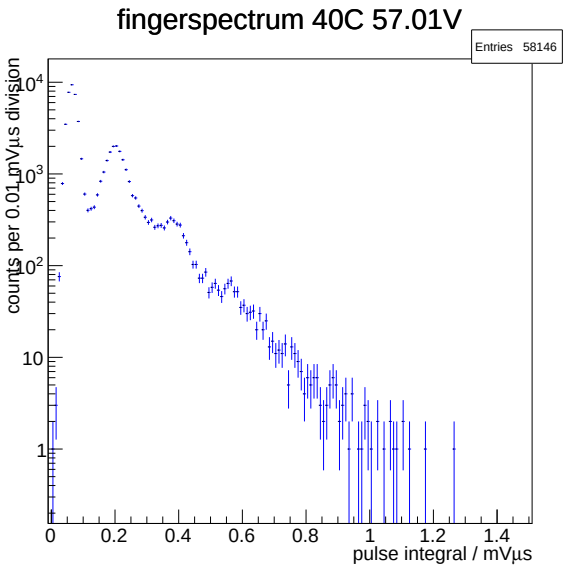

Figure 5.7: Finger spectrums of the gain method at 3.6 V overvoltage (according to the manufacturer specifications). The red dashed line marks the start of the fit range. In some spectrums a peak before the 1 p.e. finger can be observed due to misidentified noise. In the finger spectrum at 40 °C the fingers are only slightly observable due to the high dark noise rate.

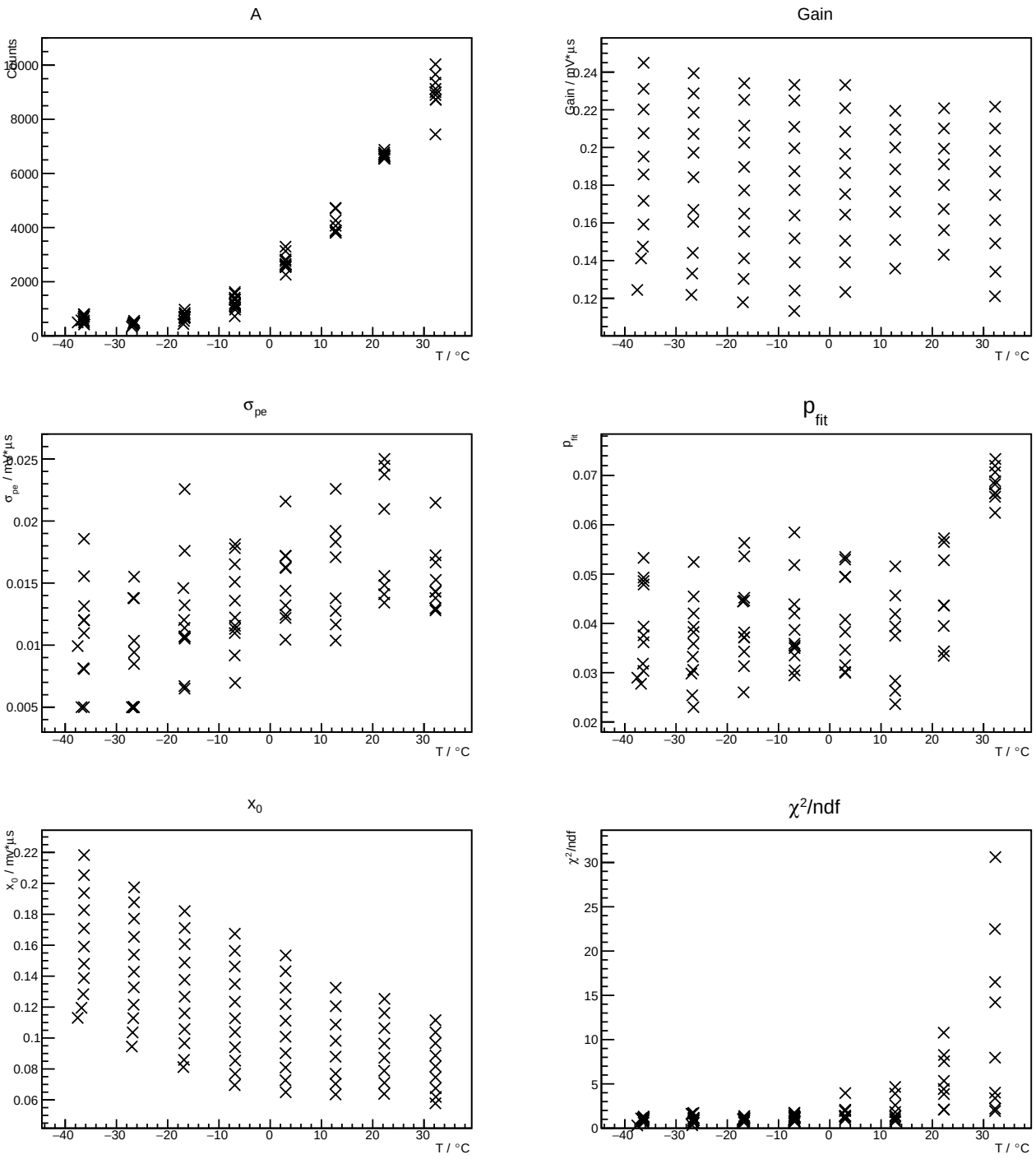

Figure 5.8: Fit results of FACT spectrum function with exponential background for all temperatures and voltages. Parameters from top left to bottom right: A, g, $\sigma_{\text{p.e.}}$, p_{fit}, $\frac{\chi^2}{\text{ndf}}$

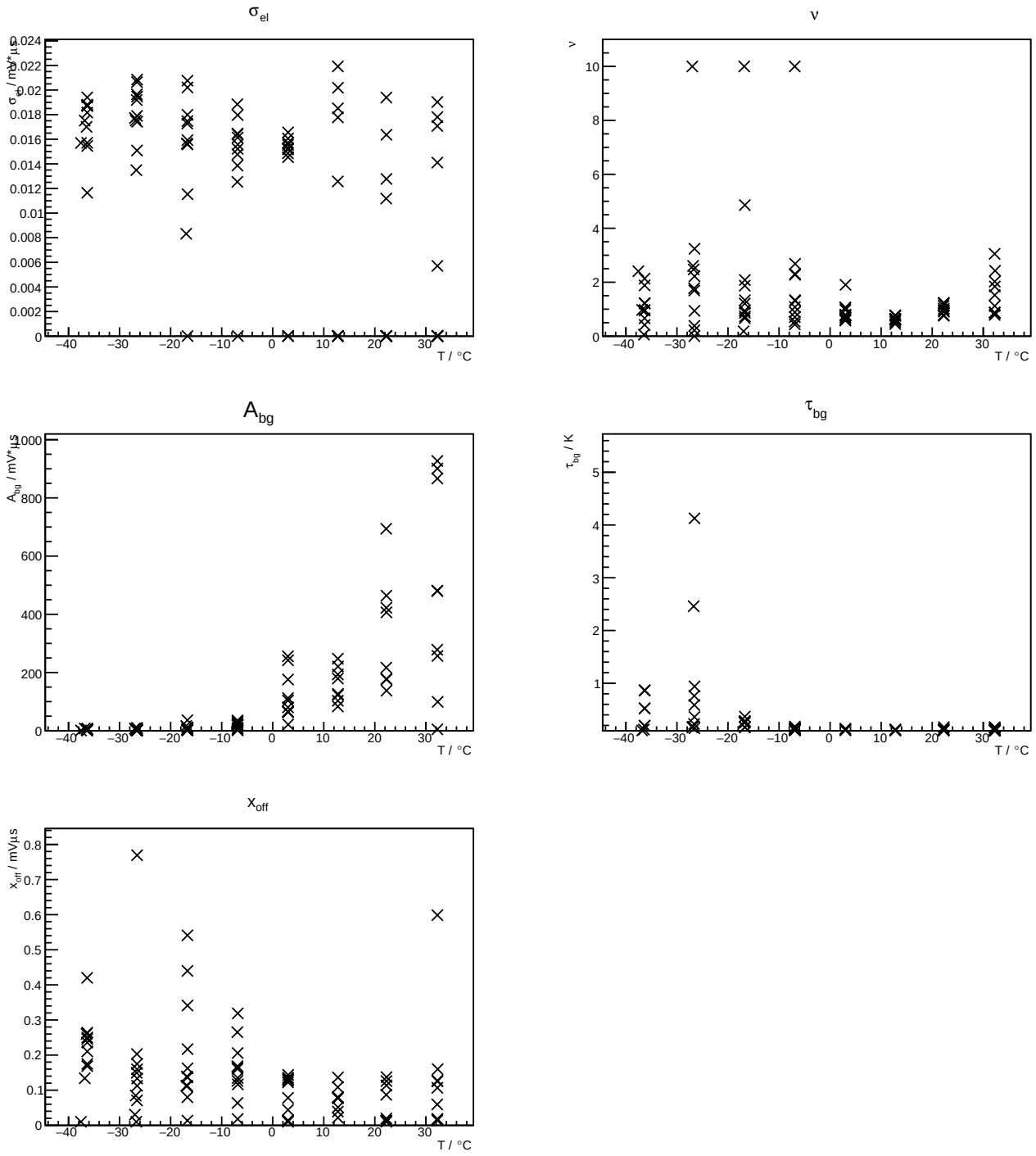

Figure 5.9: Fit results of FACT spectrum function with exponential background for all temperatures and voltages. Parameters from top left to bottom right: σ_{el}, ν, A_{bg}, τ_{bg}

- The fit results for the amplitude A double about every 10 °C, which can be explained by an increase of the dark noise rate with increasing temperature .

- The results of the gain are in similar ranges for the different temperature. This is due to the fact that the voltage range is shifted by the manufacturer specification of the progression factor β. The absence of points at temperatures over 10 °C is because some measurements at the low overvoltages had to be neglected, due to the low signal to noise ratio in the traces.

- The parameters $\sigma_{\text{p.e.}}$ and σ_{el} vary in the same range over the measured temperature range, whereas an increase with increasing bias voltage is observed.

- The parameter p_{fit} also increases with the bias voltage by $\approx \frac{0.03}{2\,\text{V}}$ which translates to an increase of the crosstalk probability with increasing temperature.

- ν is observed to increase with the bias voltage.

- The background increases similar to the amplitude A with the temperature, which can be seen at the parameter A_{bg}. The $\frac{\chi^2}{\text{ndf}}$ is near to 1 for the lower temperatures, but increases strongly at 30 °C. This indicates the limit of the peak finding algorithm's capabilities due to the increasing dark noise rate.

The error of the gain is estimated by fit error since the $\frac{\chi^2}{\text{ndf}}$ indicates a conformance of the fit with the data. The error of the bias voltage is estimated by the RMS of the 100 logged voltage values measured with the voltage supply chip.

The bias voltage is plotted against the normalised gain for each temperature. This application enables a determination of the breakdown voltage directly from the y-axis intercept. The data are fitted with a linear function parametrised as:

$$V(g) = V_{\text{BD}} + a \cdot g/g_0 \tag{5.4}$$

Here is g_0 the gain at the maximum bias voltage of a measurement series.
The graph of the fits can be seen in figure 5.10. The results of the linear fits are listed in table 5.

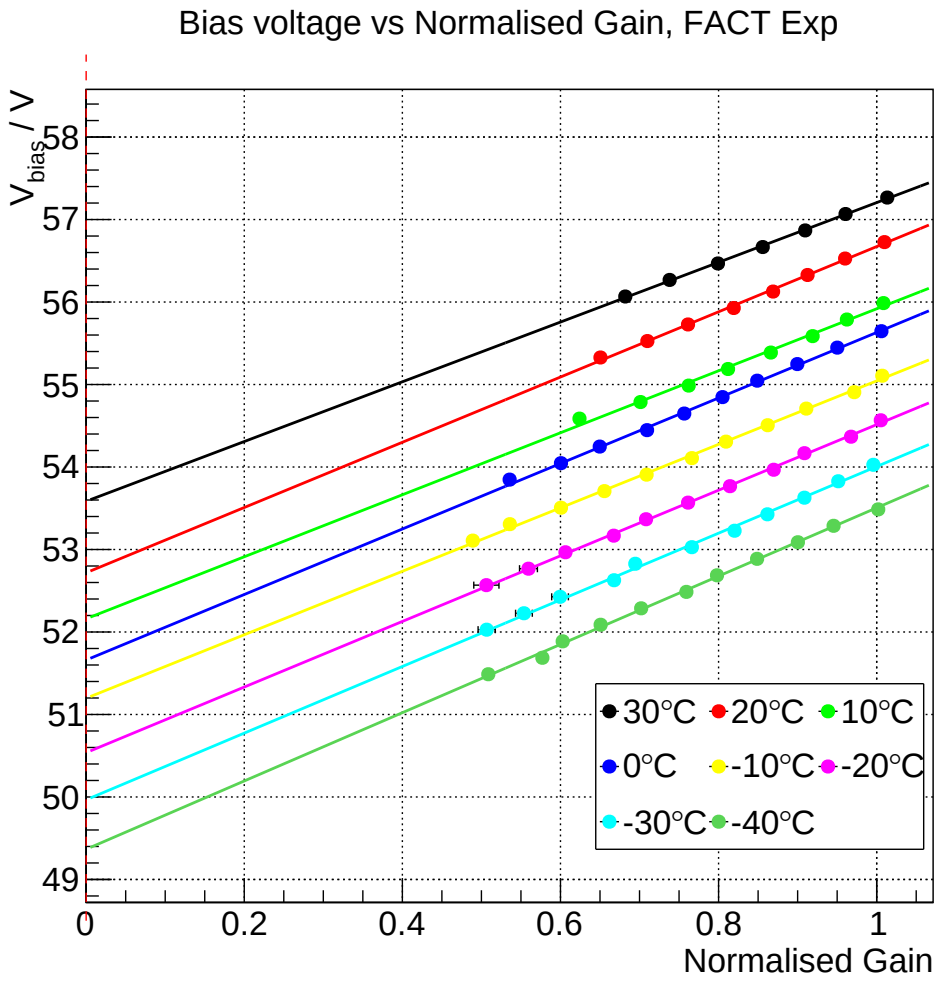

Figure 5.10: Bias voltage vs. normalised gain for temperatures from −40 °C to 30 °C. Each series of gain measurements is normed to the gain at the maximum bias voltage.

set T / °C	measured T / °C	V_{BD}/V	a	χ^2/ndf
-40	-36.05 ± 0.37	49.364 ± 0.048	4.142 ± 0.063	9.751/9
-30	-26.66 ± 0.16	49.965 ± 0.056	4.043 ± 0.069	11.524/9
-20	-16.74 ± 0.08	50.538 ± 0.050	3.967 ± 0.060	5.423/9
-10	-6.89 ± 0.03	51.198 ± 0.035	3.846 ± 0.041	16.938
0	3.00 ± 0.03	51.669 ± 0.028	3.961 ± 0.035	21.188/8
10	12.76 ± 0.02	52.182 ± 0.032	3.734 ± 0.037	62.757/6
20	22.24 ± 0.06	52.730 ± 0.029	3.944 ± 0.033	41.721/6
30	32.23 ± 0.05	53.607 ± 0.024	3.631 ± 0.028	8.06/7

Table 5: Fit results of the voltage vs. gain measurement.

With these results the breakdown voltage in in relation to the temperature can be determined. This is shown in figure 5.11. Since a linear dependence is expected, the data points are fitted by the function:

$$V_{\mathrm{BD}}(T) = V_{\mathrm{BD}}(25\,^{\circ}\mathrm{C}) + \beta \cdot (T - 25\,^{\circ}\mathrm{C}) \tag{5.5}$$

The errors of the breakdown voltages are estimated by the fit error since the $\frac{\chi^2}{\mathrm{ndf}}$ of the fits is in the order of 1. The errors on the temperature are estimated by the RMS of the logged values at one temperature.

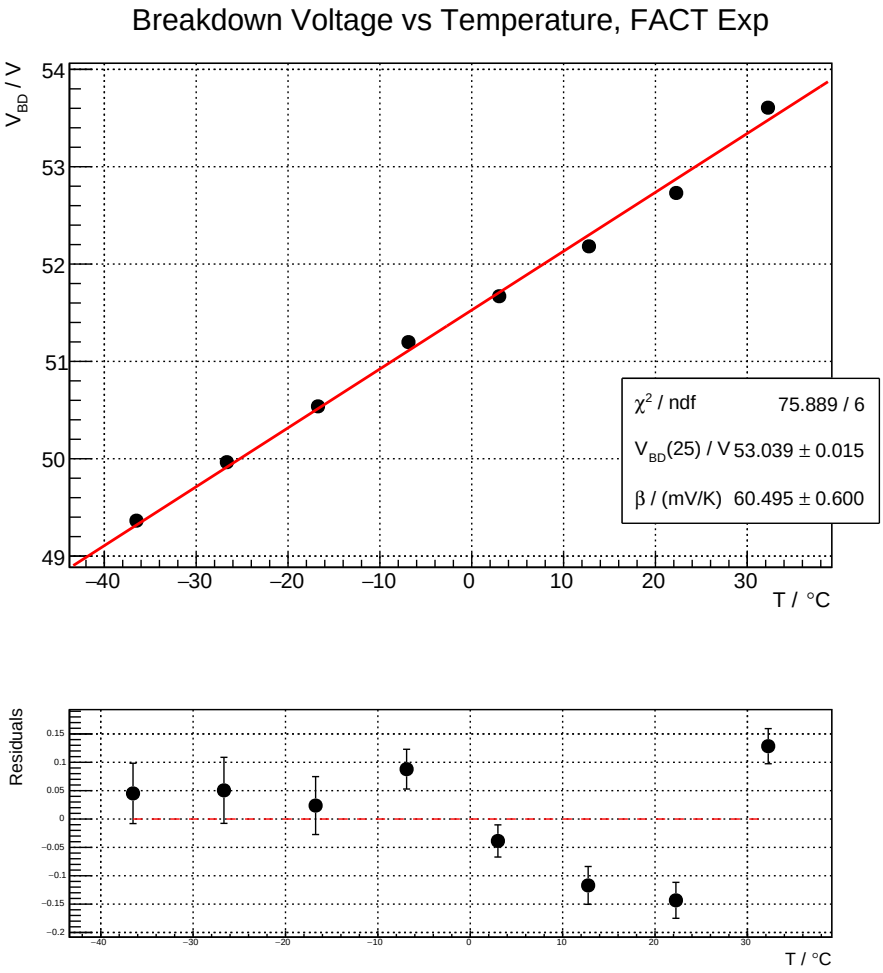

Figure 5.11: Breakdown voltage vs. temperature.

The measured breakdown voltage at 30 °C deviates from the linear dependence at the lower voltages. This is also indicated by the $\frac{\chi^2}{\text{ndf}}$ of 12.6. Therefore the fit is applied again without regarding this point. This can be seen in figure 5.12.

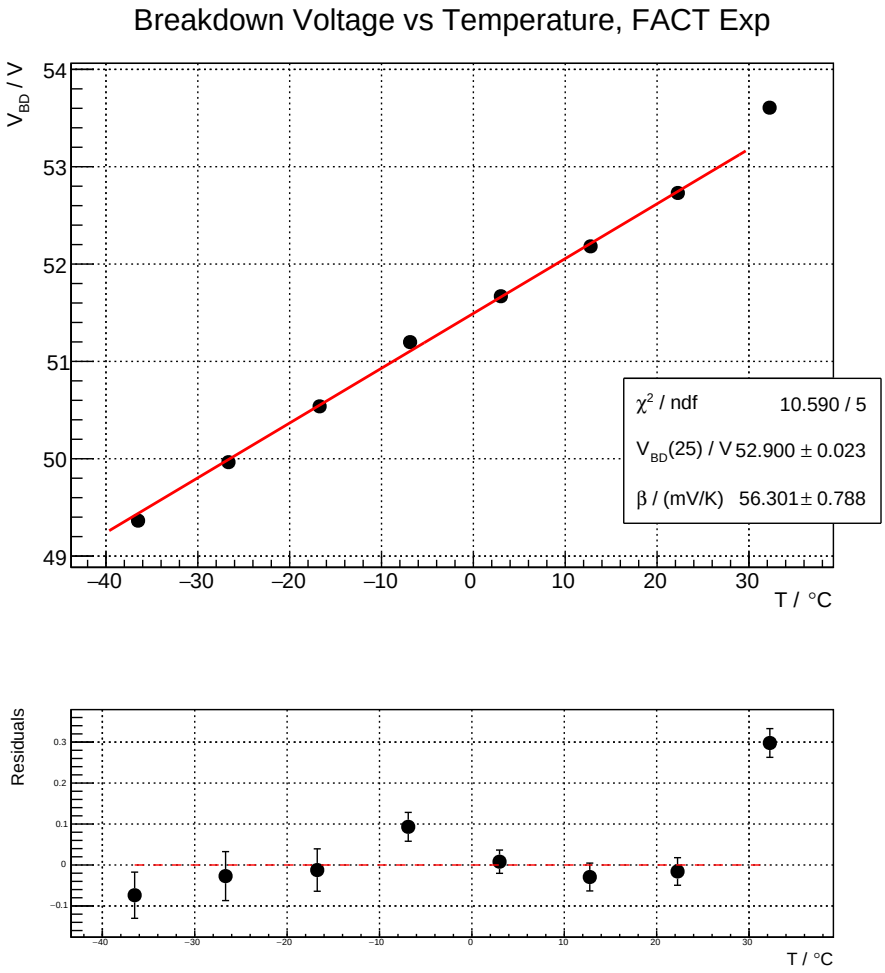

Figure 5.12: Breakdown voltage vs. temperature. The fit is applied from $-40\,°\mathrm{C}$ to $30\,°\mathrm{C}$ neglecting the up right point for the fit. The point is included in the residual fit.

By neglecting the last point the data points are well described by the linear function and the $\frac{\chi^2}{\mathrm{ndf}}$ decreases to 2.1 indicating a reasonable fit. Therefore the result of this measurement is:

$V_{\mathrm{BD}}(25\,°\mathrm{C})$	β
$(52.900 \pm 0.023)V$	$(56.30 \pm 0.79)\frac{\mathrm{mV}}{\mathrm{K}}$

Table 6: Result gain method

5.2 I-V Method

Another method to determine the breakdown voltage is to measure the I-V-curve of the SiPM. This method is used to characterise the 25 μm pitch size SiPM. As shown in [19] a similar progression factor β is expected, but also an offset between the determined breakdown voltages in the order of 100 mV.

Since the measurements are carried out in darkness, the occuring current is due to the thermal dark noise and correlated noise effects such as cross talk and afterpulses multiplied by the gain. As shown in the previous measurement the gain increases linearly with the bias voltage. The noise rate is expected to increase faster than linear with the voltage. The total increase of the current with the voltage is therefore assumed to be of the form V^n. By calculating the logarithmic derivative $\frac{d\log(V^n)}{dV} = \frac{n}{V}$ the position of the maximum of this curve is defined as the breakdown voltage V_{BD}^{DC}. [23, S.66]

5.2.1 Measurement procedure

The cathode of the SiPM is connected to the output of the power supply. The multimeter is connected in series behind the anode of the SiPM. The multimeter measures the voltage drop over its internal input resistor R_{mult} that is 10 MΩ. The current can then be calculated by $I = V_{\mathrm{mult}}/R_{\mathrm{mult}}$. This allows to measure currents in the range of nA. Because of the high resistance the voltage drop over the SiPM is calculated by the difference between the set bias voltage and the voltage drop over the resistor of the multimeter. The multimeter is connected to ground leaving the SiPM's anode floating. This measurement procedure was developed in personal correspondence with L. Middendorf and J. Schumacher at III. Phys. Inst. A at the RWTH Aachen. A schematic of the setup can be seen in figure 5.13.

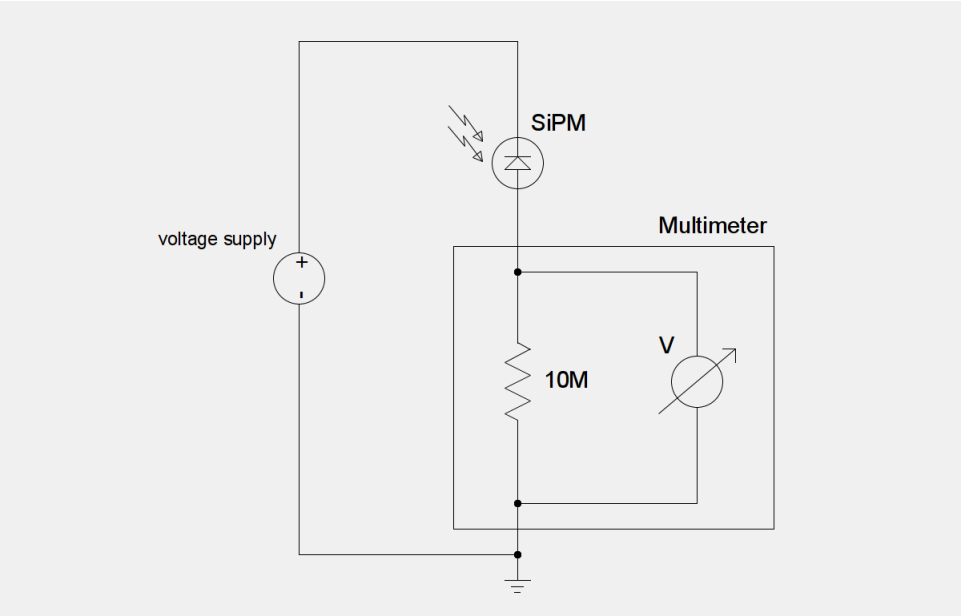

Figure 5.13: Schematic of the I-V-method

The bias voltage is increased in steps of 25 mV in a range of 1 V around the manufacturer's specification of the breakdown voltage. Each voltage is measured 20 times and the mean value of the bias and multimeter voltage is calculated. Before the set of a new bias voltage 10 seconds of waiting time are included into the measurement program to skip onset oscillations of the voltage supply. The error of the bias voltage is estimated by the RMS of the 20 values. The error of the multimeter voltage is estimated by the RMS combined with the error given by the manufacturer as listed in table 2. A voltage division of 10 V is used. The relative error of the bias voltage is $< 4\,‰$. The relative error of the current measurement is $\approx 5\%$ and thus dominates the measurement uncertainty.

The measurement is performed at temperatures from 50 °C to −30 °C in temperature steps of 10 K. The temperature is logged at every measurement point and mean value and RMS are calculated.

5.2.2 Results I-V Method

To determine the extremum in the derivative curves, a Gauss function is fitted to the peak. The fit range is $V_{\text{max}} - 0.45\,V$ to $V_{\text{max}} + 0.45\,V$, whereas V_{max} is the position of the maximum of the logarithmic derivative. The I-V-curves such as their logarithmic derivative for both SiPMs are shown in figure 5.14The high errors of the derivative result from propagating the errors to the logarithm.

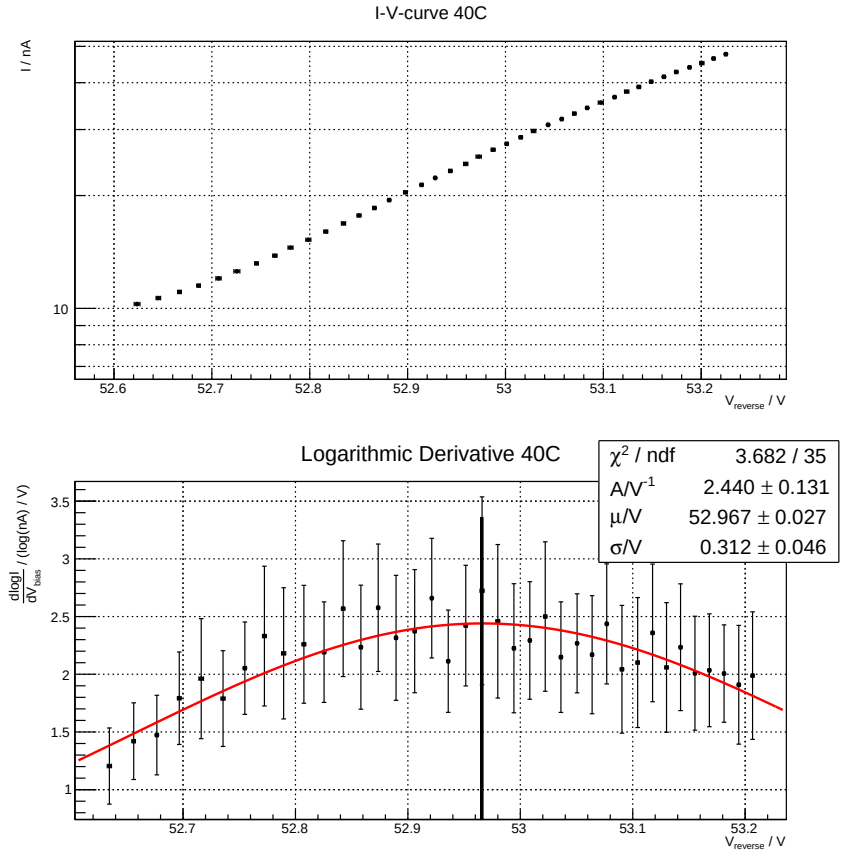

Figure 5.14: I-V-curve and logarithmic derivative of 25 μm pitch size SiPM at 0 °C. I-axis is in logarithmic scale. The black line marks the fit result for the breakdown voltage.

The breakdown voltage determined for different temperatures and a linear function parametrised by

$$V_{\mathrm{BD}}(T) = V_{\mathrm{BD}}(25\,^{\circ}\mathrm{C}) + \beta \cdot (T - 25\,^{\circ}\mathrm{C})$$

is fitted to the data. This is shown in figure 5.15.

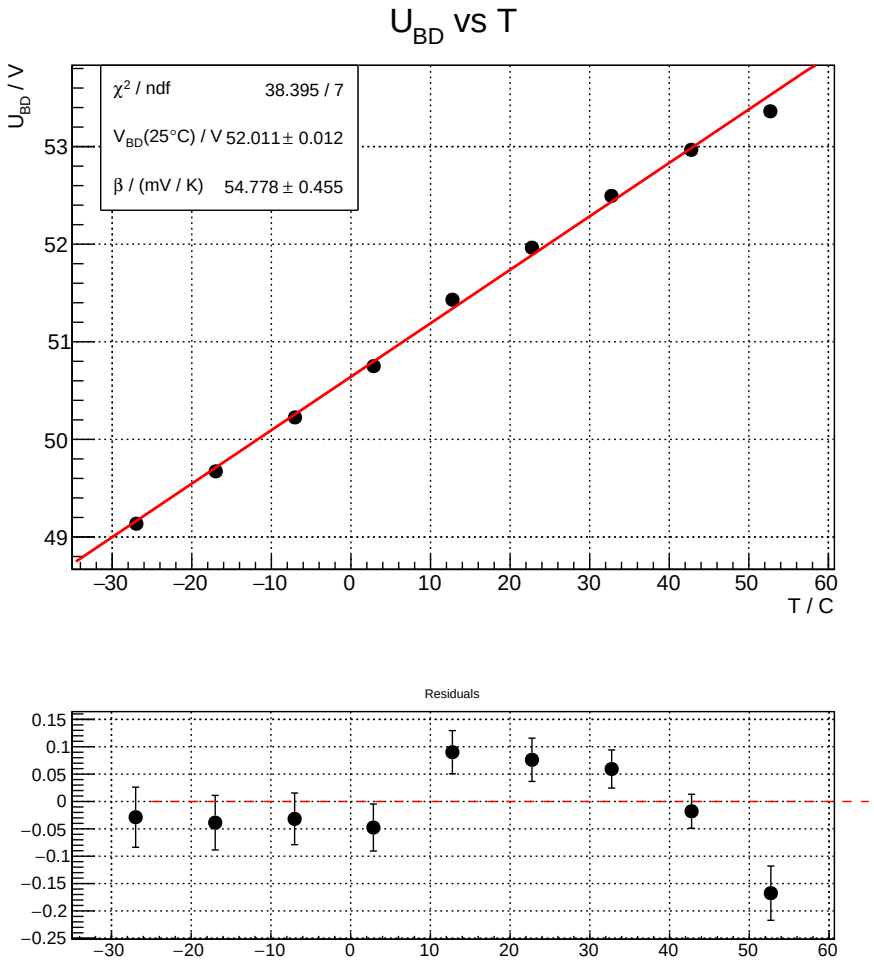

Figure 5.15: Breakdown voltage in dependence of the temperature for the 25 μm pitch size SiPM, *I-V* method.

Within the scope of the errors the data points are described by the linear function. The results of this measurement are:

$V_{\mathrm{BD}}(25\,^{\circ}\mathrm{C})$	β
$(52.011 \pm 0.012)V$	$(54.78 \pm 0.46)\frac{\mathrm{mV}}{\mathrm{K}}$

Table 7: Result *I-V*-method

The breakdown voltage at 25 °C is compatible with the manufacturers specification given in table 1. The progression factor β is within a 1.67 σ environment compatible with the measured β of the gain method of the 50 μm pitch size SiPM.

CHAPTER 6

Temperature Dependence of the Voltage Supply Chip

When measuring the temperature dependence of the front-end electronics, a contributing source is the temperature dependence of the voltage supply chip. The manufacturer claims a temperature stability of 10 ppm/K. In this section the measurement of the output voltage of the voltage supply chip is described.
For this measurement no SiPM is connected to the amplifier board. A constant voltage of 55.5 V is set and the SSD-board is placed in the climate chamber. The temperature is decreased from 50 °C to −30 °C in steps of 10 K. The output voltage V_{out} is measured by the supply chip and is logged every 5 seconds. The actual output voltage is measured with the multimeter 3.4. Its data is logged on an USB-Stick with a sample frequency of 2 Hz. A voltage range of the multimeter of 100V is used. The measurement is carried out with both versions of the SSD-electronics.
Figure 6.1 shows the results of the measurements.

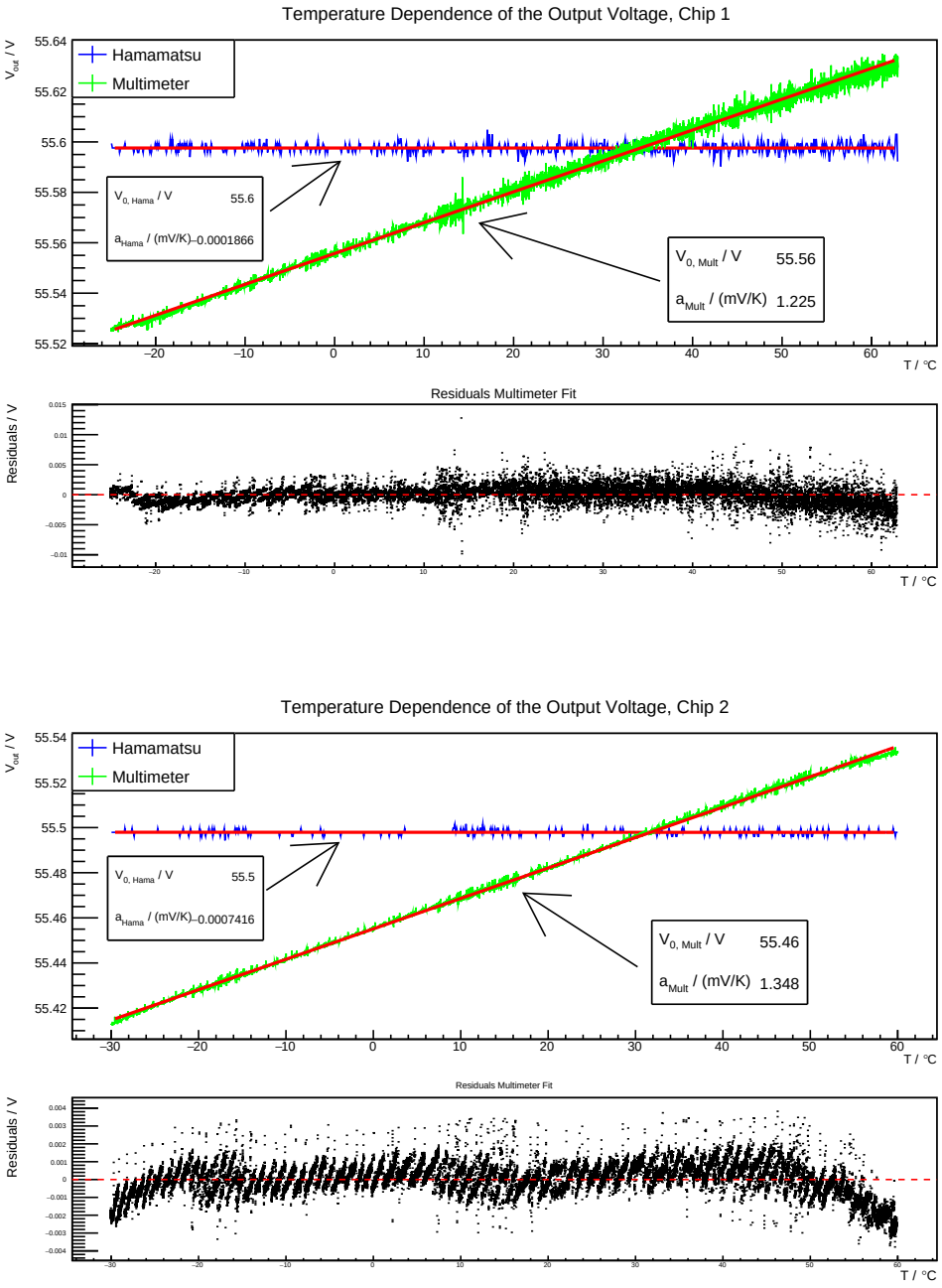

Figure 6.1: Output voltage of the power supply chips of the first and second electronics in dependence of the temperature. The voltage is measured with the supply chip (blue) and the multimeter (green). The residuals correspond to the linear fit of the multimeter data.

The two voltage measurements differ from each other. While the voltage measured by the supply unit is constantly equal to the set value over the full temperature range,

a linear increase of the voltage with the temperature is observed in the multimeter data. Both of the data sets are fitted in a range of −25 °C to 63 °C (−30 °C to 60 °C). The fit function is parametrised by $V(T) = V_i(0\,°\mathrm{C}) + a_i \cdot T$. The residuals show a statistical fluctuation around the fit. The errors of the multimeter voltage are calculated as in table 3.4. For the measured voltage range they are $\approx 0.0027\,\mathrm{V}$. Taking these errors into account the data points match well with the fitted function.
From the fit results the actual output voltage of the supply unit can be calculated by:

$$V_{\mathrm{out}} = V_{\mathrm{set}} + a \cdot (T - T_0) \tag{6.1}$$

Whereas T_0 is the temperature at which both voltages are equal and a is the sum of the slopes.

For the two board the results are:

Board	$T_0/°\mathrm{C}$	$a/\frac{\mathrm{mV}}{K}$
1	32.66	1.225
2	29.66	1.347

Table 8: Result parameters for the calculation of the output voltage of the voltage supply chip according to equation 6.1.

In conclusion a temperature stability of 22.1 ppm/K for the first board and 24.2 ppm/K for the second board was observed in the fitted range. This is twice the factor specified by the manufacturer.

CHAPTER 7

Automatised Gain Stabilisation

7.1 Measurement Setup

By programming the measured β factor into the voltage supply chip, the bias voltage is adjusted automatically in dependence of the temperature to achieve an automatised gain stabilisation.

For the measurement of the function of the automated gain stabilisation the same setup is used as for the gain method. The measured β-factor is programmed to the chip according to function 6.1. The operating voltage is set to the manufacturer recommendation that is 55.62 V at 25 °C. The measurements are carried out with the second amplifier board. The temperature is set in a range from 30 °C to −30 °C. To achieve higher statistics the number of traces is increased by 100 every temperature step, starting with 400 traces at 30 °C.

7.2 Results of the Automatised Gain Stabilisation

The traces are analysed with the same algorithm that was used for the gain method. The pulse detection parameters were adjusted in correspondence to the higher gain of the second amplifier board. The finger spectrums are fitted with the FACT spectrum function with the exponential background as also used for the gain method.

A first test of the gain stability was performed with the progression factor set to $58.26\,\frac{\mathrm{mV}}{\mathrm{K}}$. This value origins from a previous analysis of the gain method. The resulting gain in dependence of the temperature is shown in figure 7.1. The finger spectrums can be found is the appendix 9.9.

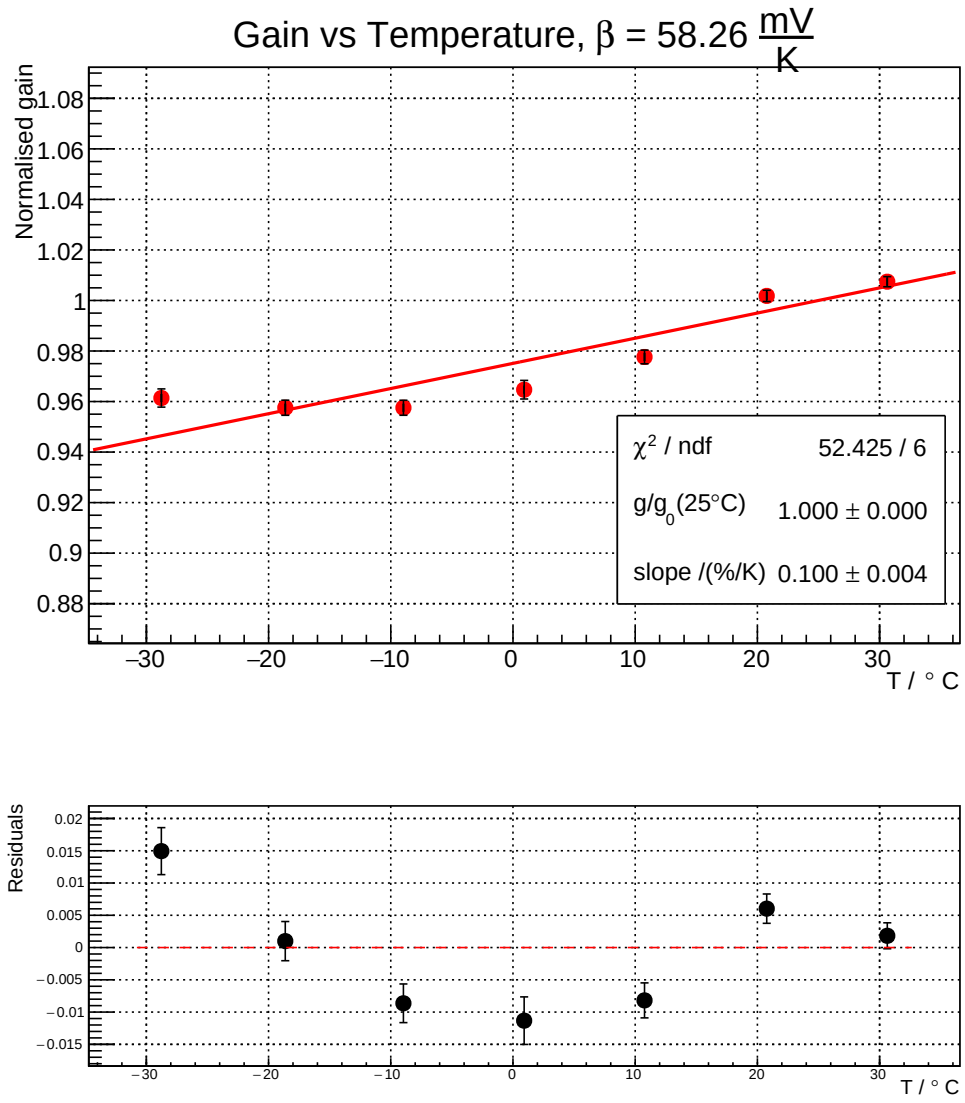

Figure 7.1: First test of automated gain stabilisation. The correction factor is set too high, because the gain increases with the temperature.

The gain is normalised to the gain at 25 °C. The remaining temperature dependence can be calculated from the slope s of the normed gain vs temperature curve and the overvoltage according to equation 2.3. Since the application is normalised the remaining temperature dependence $\Delta\beta$ can be calculated by:

$$\Delta\beta = V_{\mathrm{OV}} \cdot s \tag{7.1}$$

The overvoltage at 25 °C is calculated by the results of the gain method (table 7):

$$V_{\mathrm{OV}} = 55.62\,\mathrm{V} - 52.90\,\mathrm{V} = 2.71\,\mathrm{V}$$

. This gives the result:

$$\Delta\beta = 2.71\,\mathrm{V} \cdot 0.0010\,\mathrm{K}^{-1} = 2.71\,\frac{\mathrm{mV}}{\mathrm{K}} \quad \rightarrow \quad \beta = 55.556\,\frac{\mathrm{mV}}{\mathrm{K}} \tag{7.2}$$

Another measurement with β set to $55.43\,\frac{\mathrm{mV}}{\mathrm{K}}$ has been performed. Again this factor results from former analysis. The resulting gain in dependence of the temperature is shown in 7.3. The corresponding finger spectrums can be found in the appendix 9.10. For comparison a measurement of the gain without temperature compensation has been performed.

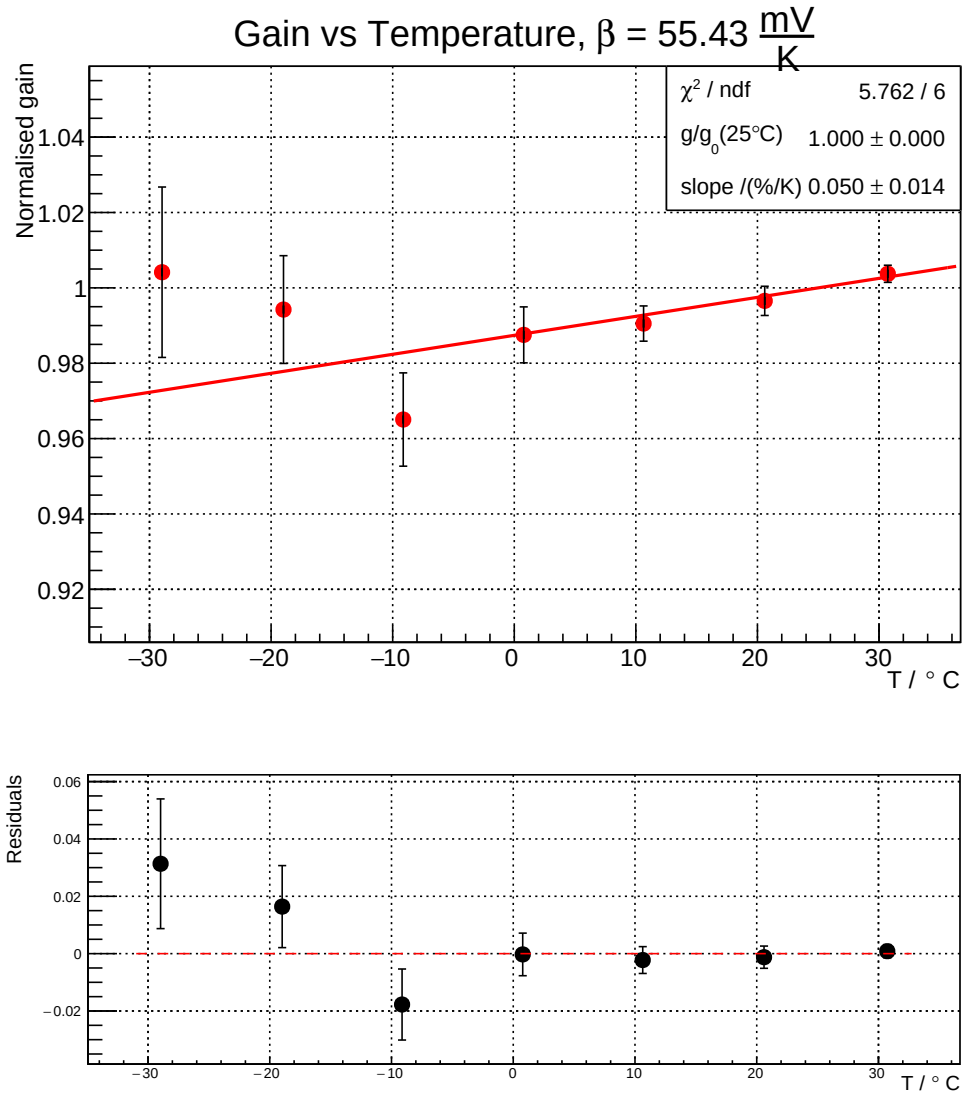

Figure 7.2: Compensated temperature dependence with a progression factor of $\beta = 55.43\,\frac{\mathrm{mV}}{\mathrm{K}}$.

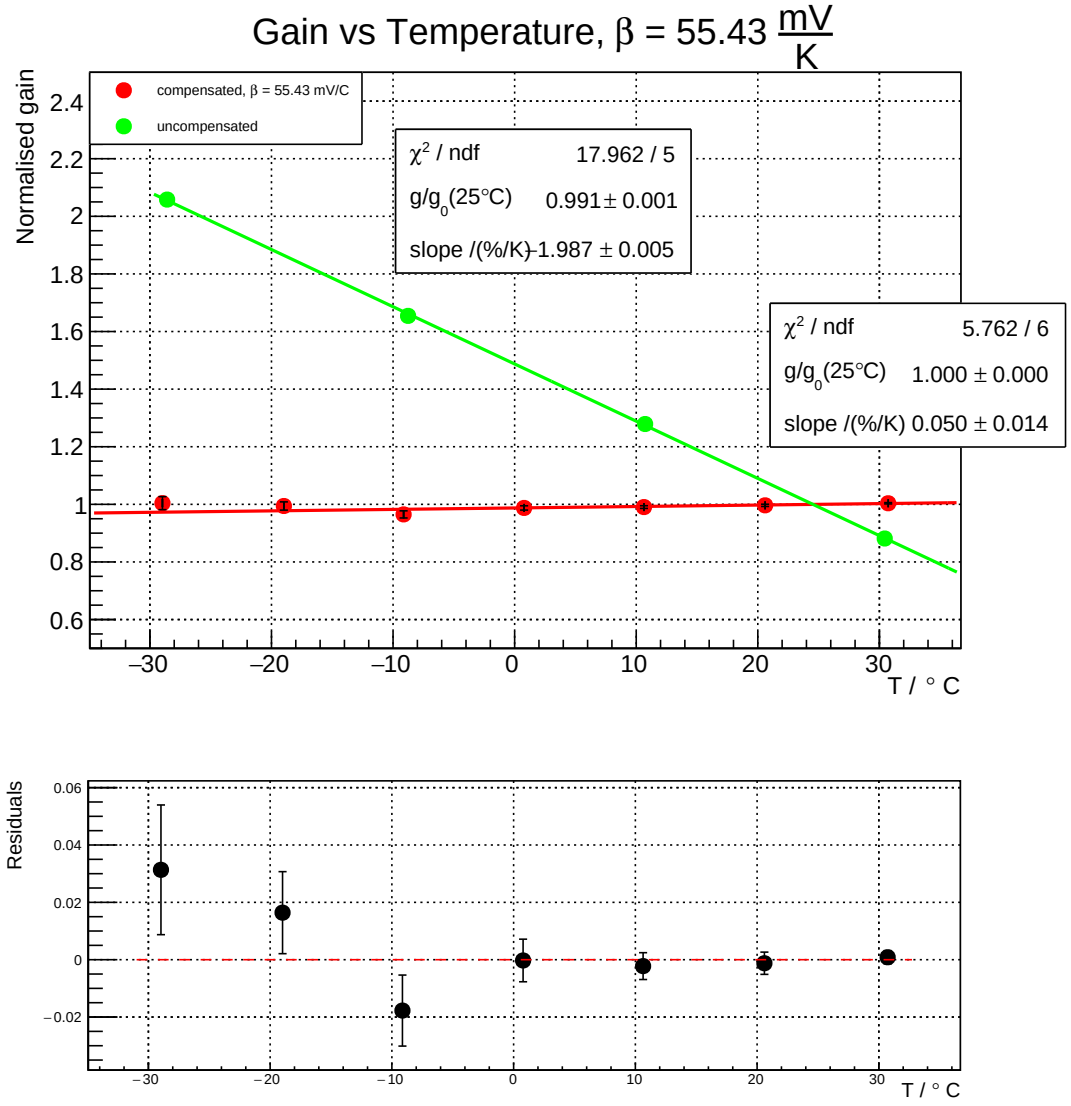

Figure 7.3: Comparison of the gain in dependence of the temperature with and without bias voltage adjustment

By setting a compensation factor of 55.43 $\frac{\text{mV}}{\text{K}}$ the gain increases by $\frac{0.05\,\%}{\text{K}}$ and less than 4 % over a temperature difference of 60 K. Again the progression factor can be corrected by the slope of the resulting fit. This results in:

$$\Delta\beta = 2.71\,\text{V} \cdot 0.00050\,\text{K}^{-1} = 1.355\,\frac{\text{mV}}{\text{K}} \quad \rightarrow \quad \beta = 54.075\,\frac{\text{mV}}{\text{K}}$$

Since the measurement time with the climate chamber was limited no further measurements of the corrected progression factor could have been carried out.

CHAPTER 8

Conclusion and Outlook

In this thesis the temperature dependence of two SiPMs with a pitch size of $50\,\mu$m and $25\,\mu$m could be measured. The $50\,\mu$m was characterised using the gain method and the $25\,\mu$m by the I-V-method. The gain method yielded a progression factor of $(56.30 \pm 0.79)\,\frac{\mathrm{mV}}{\mathrm{K}}$ and the I-V-method a factor of $(54.78 \pm 0.46)\,\frac{\mathrm{mV}}{\mathrm{K}}$. Within $1.7\,\sigma$ the values are compatible. These factors include the temperature dependence of the voltage supply chip which is $1.225\,\frac{\mathrm{mV}}{\mathrm{K}}$.

The automatised gain stabilisation that can be implemented to the voltage supply chip has been tested with different factors. The best stabilisation was achieved with a factor of $\beta = (54.43)\,\frac{\mathrm{mV}}{\mathrm{K}}$ with a remaining temperature dependence of $0.05\,\frac{\%}{\mathrm{K}}$.

In conclusion it can be said that within the scope of the possible measurement precision the temperature dependence of the SSD electronics could be compensated.

For the Auger Prime Upgrade it is necessary to know the temperature dependence for many SiPMs. For this task the measurement of the temperature dependence by the I-V- method is more practicable. In comparison to the gain method, the I-V-method requires less non-trivial analysis methods such as a peak finding algorithm and a spectrum function that correctly describes the finger spectrums. This counts especially for temperatures over $30\,^{\circ}\mathrm{C}$. Since the two methods yield similar progression factors, the I-V-method can be used to determine β coarsly at first and then do the fine adjustment by measuring the gain at a high temperature difference. However, the offset of the breakdown voltages between the two methods still has to be theoretically understood.

Danksagung

Zunächst bedanke ich mich bei Herrn Professor Bretz und Herrn Professor Hebbeker, die mir ermöglicht haben diese Arbeit an ihrem Institut anzufertigen.

Ich danke außerdem meinem Betreuer Johannes Schumacher für hilfreiche Ratschläge und die Geduld die er während der langwierigen Messungen aufgebracht hat. Außerdem danke ich der gesamten Auger Arbeitsgruppe, besonders meinen Bürokollegen Daniel und Alexander, die für ein angenehmes Arbeitsklima sorgten und immer für einen Kaffee zu haben waren.

Des weiteren danke ich Frank, in dessen Zusammenarbeit die C++ Bibliothek 'PraktLib' entstand, die an vielen Stellen Verwendung gefunden hat.

Danke auch an Nils für das zügige Korrekturlesen der Arbeit. Besonderer Dank gilt meinen Eltern, die mir während der Arbeit sowohl seelisch als auch sachlich beistanden.

Eidesstattliche Versicherung

Ich versichere hiermit an Eides Statt, dass ich die vorliegende Bachelorarbeit mit dem Titel:
'Temperature Dependence of the SiPMs and the front-end Electronics for Auger Prime' selbstständig und ohne unzulässige frende Hilfe erbracht habe. Ich habe keine anderen als die angegebenen Quellen und Hilfsmittel benutzt. Die Arbeit hat in gleicher oder ähnlicher Form noch keiner Prüfungsbehörde vorgelegen.

Ort, Datum

Christoph Günther

References

[1] Alexander Aab et al. *Searches for Large-Scale Anisotropy in the Arrival Directions of Cosmic Rays Detected above Energy of* 10^{19} *eV at the Pierre Auger Observatory and the Telescope Array*. Astrophys. J. 794.2 (2014), p. 172. DOI: 10.1088/0004-637X/794/2/172. arXiv: 1409.3128 [astro-ph.HE].

[2] Alexander Aab et al. *The Pierre Auger Observatory Upgrade - Preliminary Design Report* (2016). arXiv: 1604.03637 [astro-ph.IM].

[3] A Biland et al. *Calibration and performance of the photon sensor response of FACT — the first G-APD Cherenkov telescope*. Journal of Instrumentation 9.10 (2014), P10012. URL: http://stacks.iop.org/1748-0221/9/i=10/a=P10012.

[4] R. Brun, F. Rademakers, et al. *ROOT web page, http://root.cern.ch/*. 2001.

[5] *Datasheet Binder MK 240 Climate Chamber*. Tech. rep. Available online at www.binder-world.com/de/content/download/103775/1937021/file/Data%20Sheet%20Model%20MK%20240%20de.pdf , visited 5.7.2016.

[6] *Datasheet Fairchild BC547*. Tech. rep. Available online at https://www.fairchildsemi.com/datasheets/BC/BC547.pdf , visited 5.7.2016.

[7] *Datasheet Hamamatsu C11204-02 Power supply*. Tech. rep. Available online at https://www.hamamatsu.com/resources/pdf/ssd/c11204-02_kacc1242e.pdf , visited 5.7.2016.

[8] *Datasheet Hamamatsu S13360 series*. Tech. rep. Available online at http://www.hamamatsu.com/resources/pdf/ssd/s13360_series_kapd1052e.pdf , visited 5.7.2016.

[9] *Datasheet Texas Instruments LM94021 Analog Temperature Sensor*. Tech. rep. Available online at http://www.ti.com/lit/ds/symlink/lm94021.pdf , visited 5.7.2016.

[10] *Datasheet Texas Instruments TLC272*. Tech. rep. Available online at http://www.ti.com.cn/cn/lit/ds/symlink/tlc272.pdf , visited 5.7.2016.

[11] N. Dinu et al. *Temperature and Bias Voltage Dependence of the MPPC Detectors*. 2010 IEEE Nuclear Science Symposium, Medical Imaging Conference and 17th Room Temperature Semiconductor Detector Worksho. Poster - to appear in the IEEE Transactions on Nuclear Science. Oct. 2010. DOI: 10.1109/NSSMIC.2010.5873750. URL: http://hal.in2p3.fr/in2p3-00537108.

[12] Fluke. *8845A/8846A Users Manual* (). Available online at: http://download.flukecal.com/pub/literature/884xa___umeng0300.pdf , visited 5.7.2016.

[13] Hamamatsu. *Capabilities of Silicon Photomultipliers*. http://www.hamamatsu.com/us/en/community/optical_sensors/sipm/capabilities/index.html.

[14] Hamamatsu. *Technical Information MPPC, MPPC modules* (). Available online at https://www.hamamatsu.com/resources/pdf/ssd/mppc_kapd9003e.pdf , visited 6.7.2016.

[15] Rudolf Kränzler. *Messprotokoll Nr. 0286 Objekt: 5mm Superhelle LED UV*. Tech. rep. Available online at http://www.leds.de/out/media/15401_Messprotokoll_0286.pdf.pdf, visited 6.7.2016.

[16] Prof. Dr. Laufs, Prof. Dr. Jacques, and Dipl.-Ing. Sureck. *Praktikum Sensorsyteme*. Available online at http://old.et.fh-duesseldorf.de/home/lauffs/sensor/downloads/gest.quellen.pdf , visited 6.7.2016.

[17] LeCroy. *Wave 300A Series Osciloscopes Users Manual*. Tech. rep. Available online at: http://cdn.teledynelecroy.com/files/manuals/wj300a-gsm_reva.pdf , visited 5.7.2016.

[18] *LiB LAB project website*. Available online at: https://forge.physik.rwth-aachen.de/projects/liblab, visited 14.7.2016.

[19] Adam Nepomuk Otte et al. *Characterization of Three High Efficiency and Blue Sensitive Silicon Photomultipliers* (2016). arXiv: 1606.05186 [physics.ins-det].

[20] *Raspberry Pi Homepage*. https://www.raspberrypi.org/.

[21] Steven H Simon. *The Oxford solid state basics*. Oxford, UK: Oxford Univ. Press, 2013. URL: https://cds.cern.ch/record/1581455.

[22] *WiringPi - GPIO Interface library for the Raspberry Pi*. Available online at: http://wiringpi.com/ , visited 20.6.2016.

[23] Chen Xu. *Study of the Silicon Photomultipliers and Their Applications in Positron Emission Tomography*. University of Hamburg, Diss., 2014. Dr. Hamburg: University of Hamburg, 2014, p. 119. URL: https://bib-pubdb1.desy.de/record/168988.

CHAPTER 9

Appendix

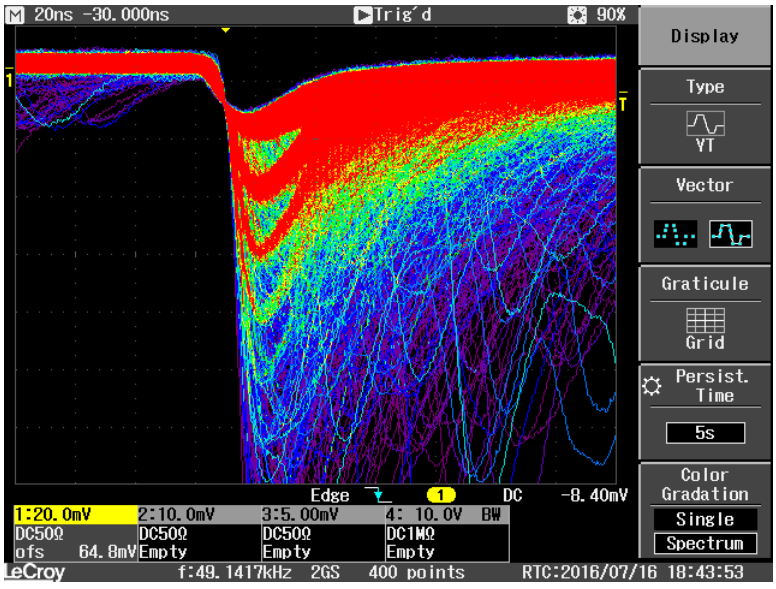

Figure 9.1: Oscillogram, −30 °C, 57.00 V

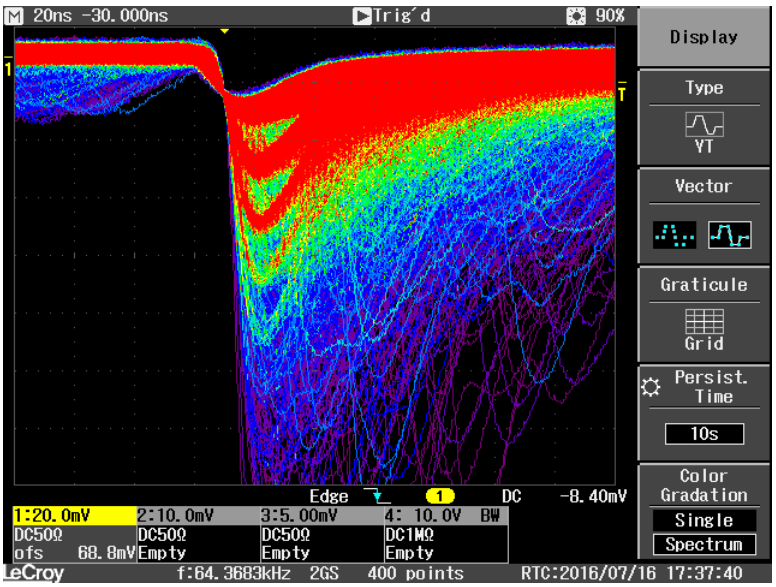

Figure 9.2: Oscillogram, −20 °C, 57.00 V

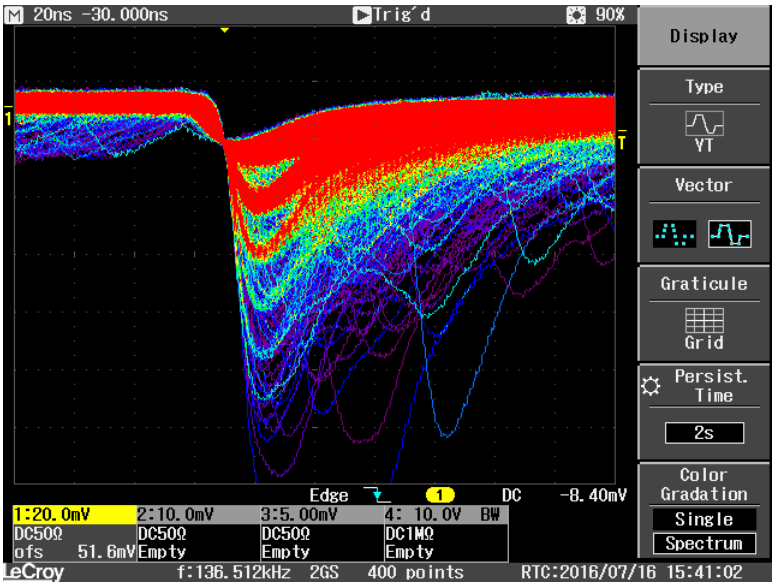

Figure 9.3: Oscillogram, −10 °C, 57.00 V

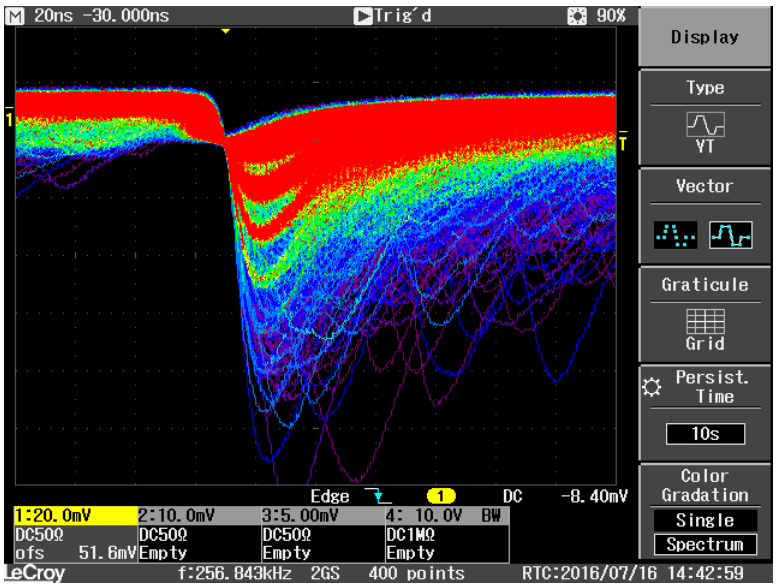

Figure 9.4: Oscillogram, 0 °C, 57.00 V

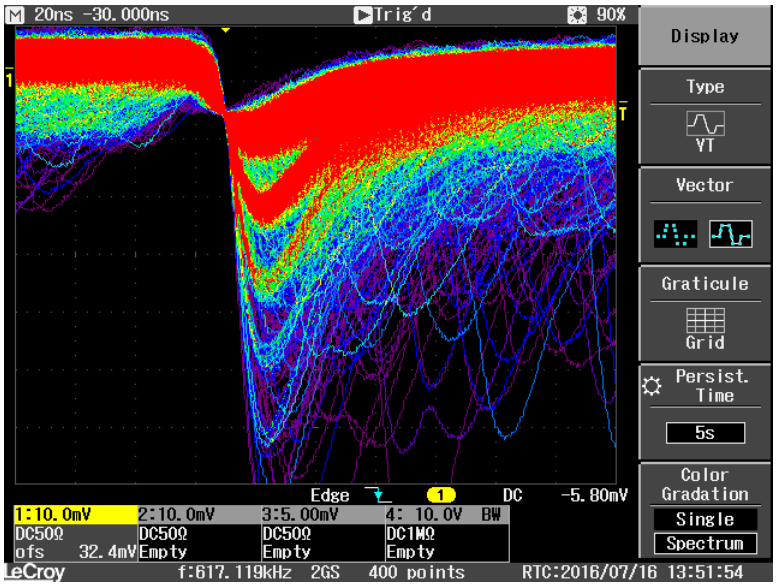

Figure 9.5: Oscillogram, 10 °C, 57.00 V

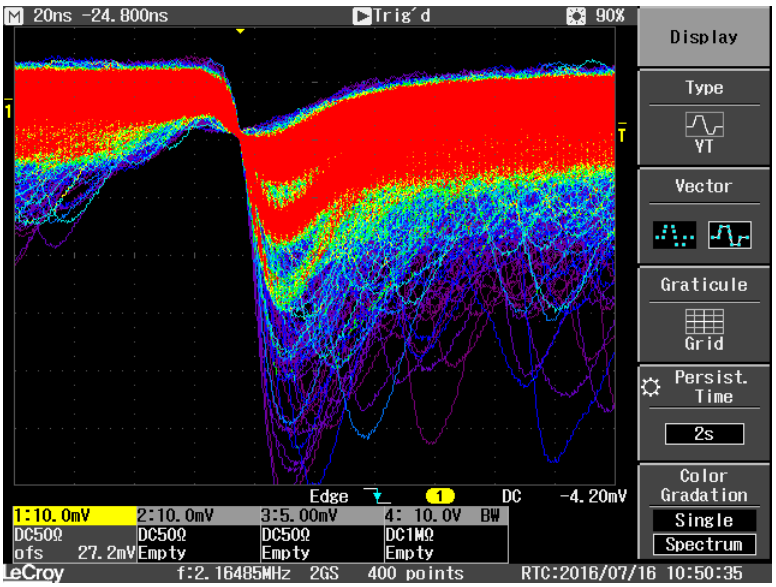

Figure 9.6: Oscillogram, 20 °C, 57.00 V

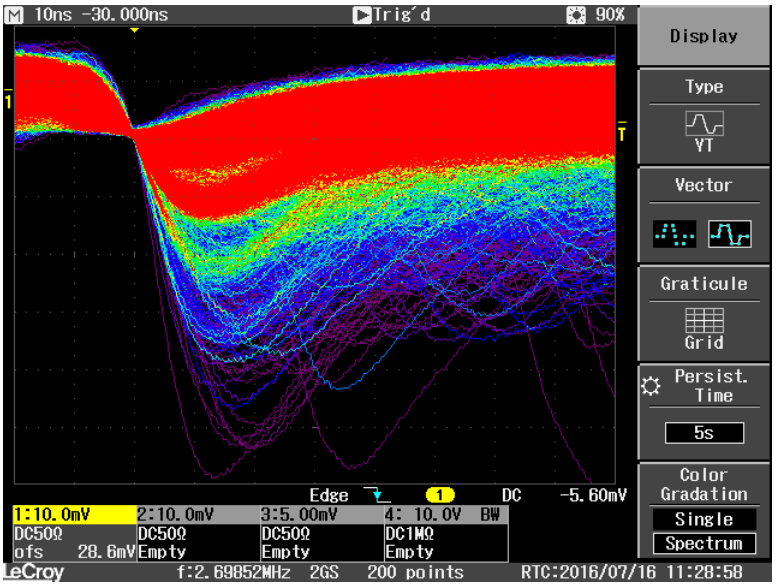

Figure 9.7: Oscillogram, 30 °C, 57.00 V

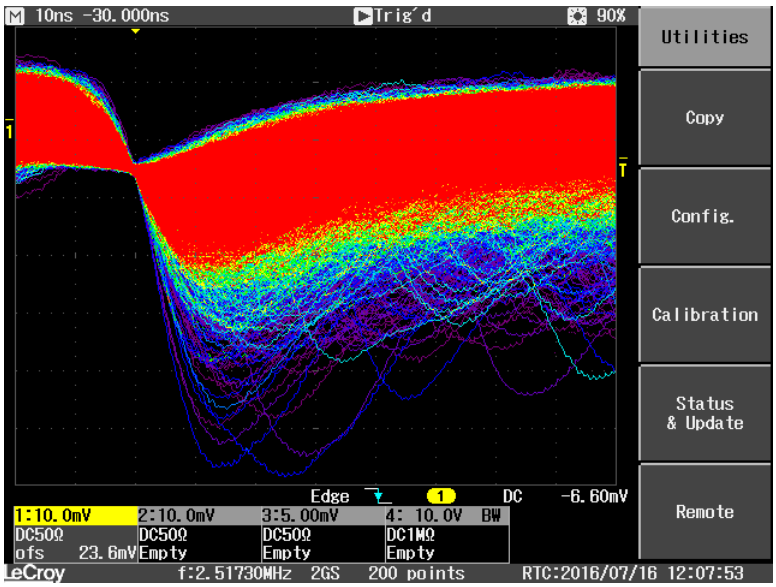

Figure 9.8: Oscillogram, 40 °C, 57.00 V

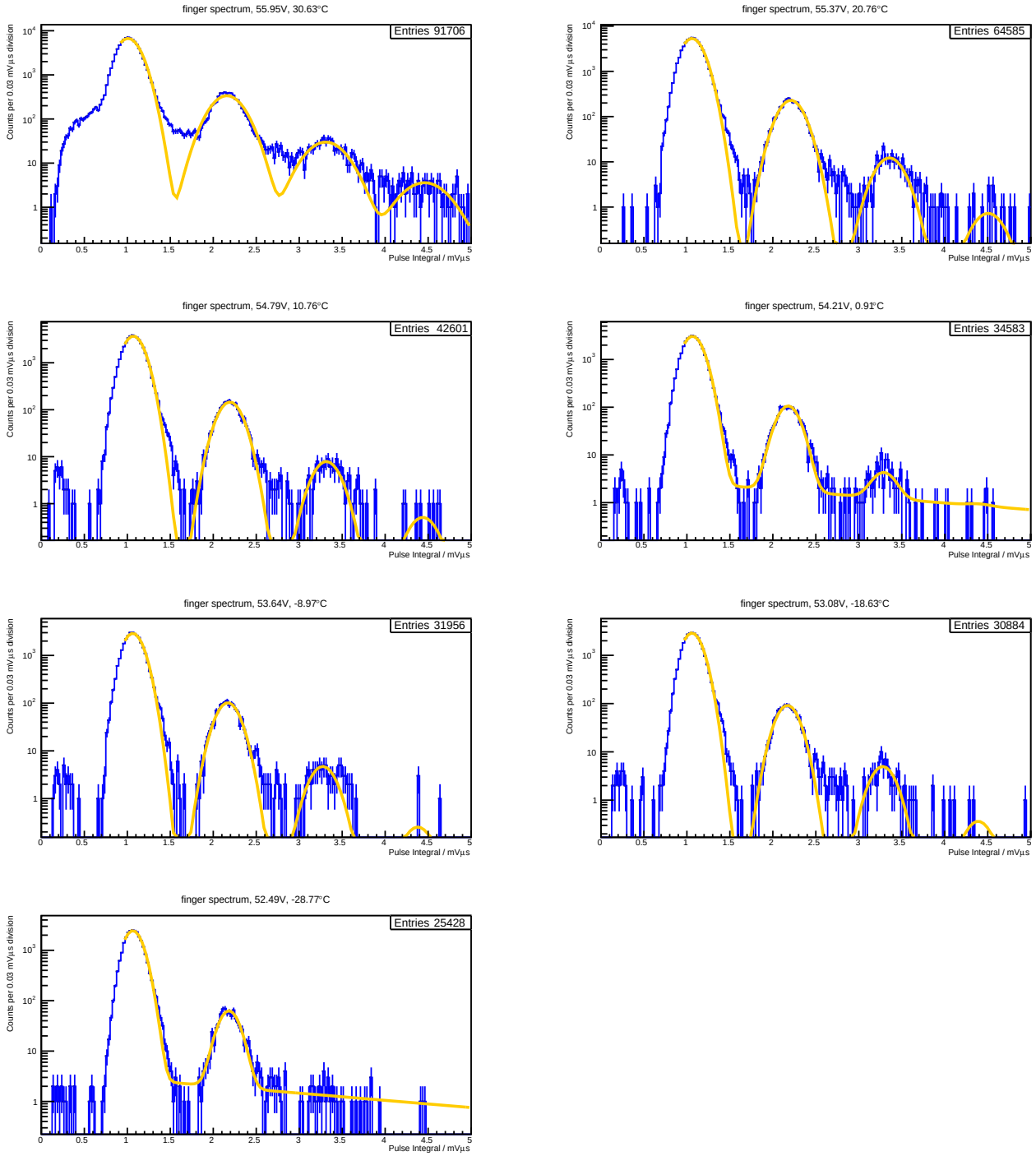

Figure 9.9: Finger spectrums for $\beta = 58.26\ \frac{\mathrm{mV}}{\mathrm{K}}$

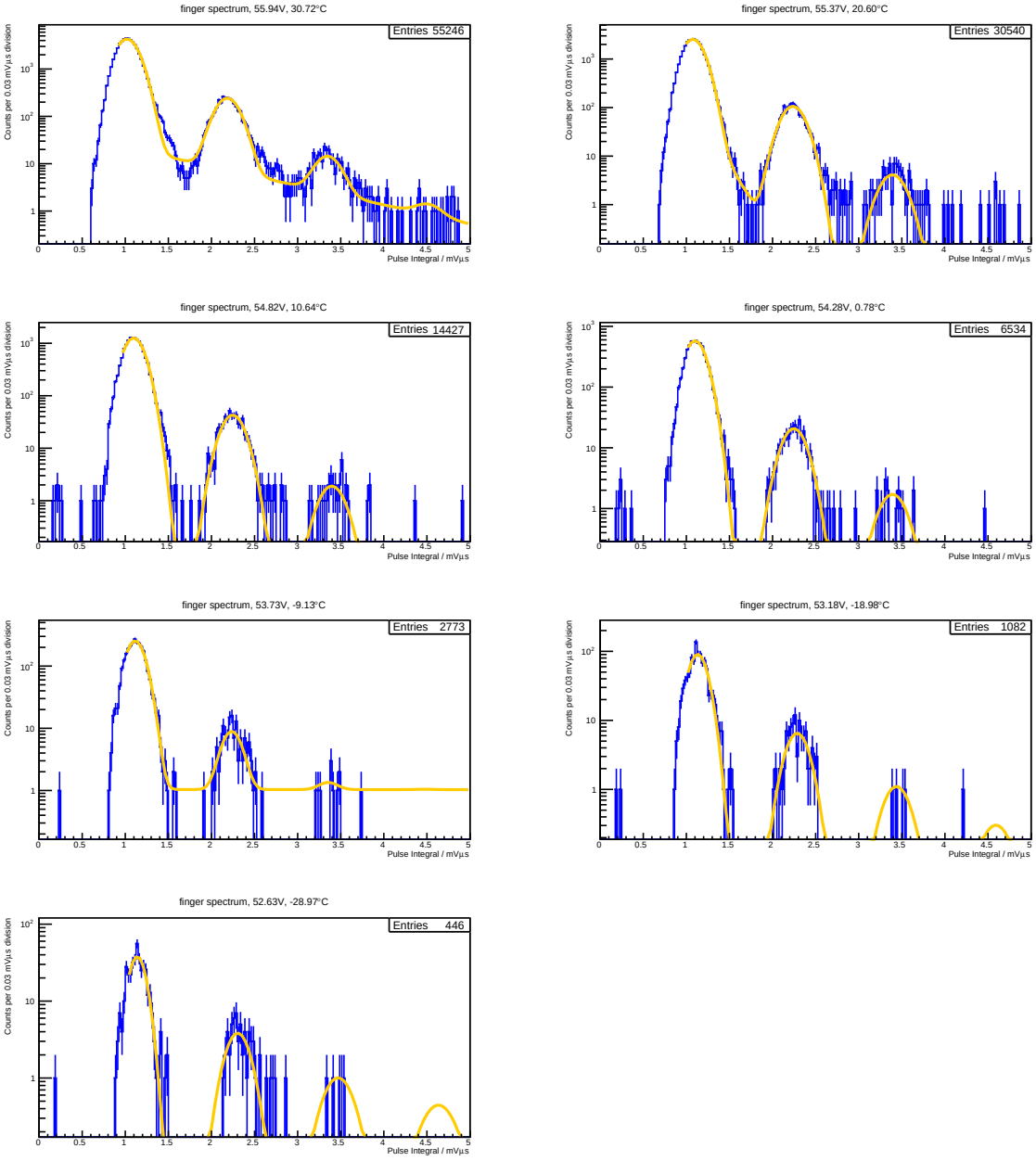

Figure 9.10: Finger spectrums for $\beta = 55.43\,\frac{\mathrm{mV}}{\mathrm{K}}$